Enhanced band gap energy of one-pot mechano-synthesized Ag_3PO_4 for Orange G photodegradation under visible light irradiation

An in-depth experimental and DFT studies

Ait Baha, Ali; Khossossi, Nabil; Lakbita, Omar; Brahmi, Younes; El Mernissi, Yassine; Aziz, Taoufyq; Benlhachemi, Abdeljalil; Bakiz, Bahcine; Abou Oualid, Hicham

DOI
10.1016/j.cplett.2024.141681

Publication date
2024

Document Version
Final published version

Published in
Chemical Physics Letters

Chemical Physics Letters 856 (2024) 141681

Contents lists available at ScienceDirect

Chemical Physics Letters

journal homepage: www.elsevier.com/locate/cplett

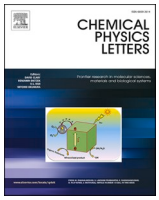

Enhanced band gap energy of one-pot mechano-synthesized Ag_3PO_4 for Orange G photodegradation under visible light irradiation: An in-depth experimental and DFT studies

Ali Ait Baha [a,e], Nabil Khossossi [b], Omar Lakbita [c], Younes Brahmi [d], Yassine El Mernissi [e], Taoufyq Aziz [a], Abdeljalil Benlhachemi [a], Bahcine Bakiz [a], Hicham Abou Oualid [e,*]

[a] Materials and Environment Laboratory (LME), Department of Chemistry, Faculty of Sciences, University Ibn Zohr, Agadir 80000, Morocco
[b] Department of Materials Science and Engineering, Faculty of Mechanical, Maritime and Materials Engineering, Delft University of Technology, Mekelweg 2, 2628 CD Delft, Netherlands (the)
[c] Applied Chemistry & Engineering Research Centre of Excellence (ACER CoE), Mohammed VI Polytechnic University (UM6P), Lot 660 – Hay Moulay Rachid, Benguerir 43150, Morocco
[d] Mohammed VI Polytechnic University (UM6P), HTMR-Lab, 43150 Benguerir, Morocco
[e] Green Energy Park, IRESEN-UM6P, Benguerir, Morocco

ARTICLE INFO

Keywords:
Photocatalysis
Ag_3PO_4
Mechanochemical method
DFT calculations
Band gap energy- Orange G

ABSTRACT

The present study highlights the efficiency of Ag_3PO_4 photocatalyst with a band gap of 2.25 eV, synthesized by a green and one-pot simple mechanochemical method, towards photodegradation of orange G under visible irradiation. The phase structure, morphology, and optical properties of mechano-synthesized Ag_3PO_4 were investigated using X-ray diffraction, Scanning Electron Microscopy, Thermogravimetric Analysis, Fourier Transform Infrared, the Brunauer-Emmet-Teller surface area, and UV–vis diffuse reflectance spectroscopy. DFT calculations were also conducted for band gap energy prediction. The photocatalytic activity of the sample was evaluated using a central composite design for surface response methodology (CCD-RSM) to determine the optimal conditions for Orange G (OG) removal. The photocatalytic activity of Ag_3PO_4 was approximately 93 % within 20 min of reaction under irradiation for 24.6 mg/L and 11 mg/L of Ag_3PO_4 and Orange G, respectively. Trapping experiments confirmed that peroxides and hydroxyl radicals are the dominant active species in the photodegradation process.

1. Introduction

Because of population and economic growth resulting in natural resources depletion, valorization of these sources has been becoming a necessity not only to synthesize sustainable materials and producing bio-energy as well, but also to cope with environmental issues such as pollution [1,2]. Water constitutes a fascinating substance in our life and its treatment by removing dye pollutants that affects negatively both human health and ecosystem, is an outstanding topic [3]. To this end, researchers counted on several technologies to deter with this specific problem, such as ion exchange removal [4], ozonation [5], catalytic reduction [6], adsorption [7], coagulation [8],biological/aerobic treatment [9], membrane filtration [10,11] and photo-catalysis [12,13,14,15,16]. This letter consisting of an advanced and common technology, involves the absorption of light by semiconductor particles that intervening thereafter to through an oxidation reaction to eliminate dangerous compounds from wastewater [17,18,19]. The evolution of photocatalysis technique started when Fujishima and Honda worked on TiO_2 electrode photocatalyst for water splitting [20]. Nevertheless, though various polymorphic forms this material has (rutile 3.0 eV, anatase 3.2 eV, and brookite 3.3 eV), it cannot be used as a visible light photocatalyst. Thence, its modification by doping and parameters influencing its photocatalytic activity were investigated [21].

In this context,phosphate based semiconducting materials are widely used in photocatalysis [22,23,24,25], supercapacitors [26] and electrocatalysis [27]. Their prominence as photocatalysts is ascribed to their attractive optical properties including band gap energy. The band gap energy of a semiconductor is the required energy for an electron

* Corresponding author.
E-mail address: abououalid@greenenergypark.ma (H. Abou Oualid).

https://doi.org/10.1016/j.cplett.2024.141681
Received 21 July 2024; Received in revised form 24 September 2024; Accepted 8 October 2024
Available online 11 October 2024

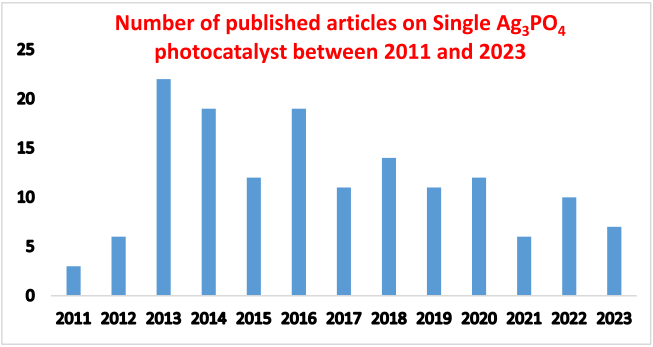

Fig. 1. Ag_3PO_4 publications from 2011 to 2023.

transition from valence band to the conduction band, and its calculation is a key to anticipate photophysical and photochemical properties of semiconductors [28].

Among these materials, silver phosphate has drawn much attention after its discovery as a visible light active photocatalyst thanks to the indirect band gap energy that was found to be 2.4 eV. The striking photo-catalytic activity of this material is ascribed to its electronic structure, contributing to the maintaining of a large dipole in Ag_3PO_4, leading to the distortion of AgO_4 tetrahedral as well as to the separation of (e^-/h^+) pairs by attracting holes and repulsing electrons. Moreover, it is suggested that Ag defects will allure photo-excited holes owing to their unoccupied states, and then hinder the recombination of (e^-/h^+) pairs [29,30,31].

By virtue of the interesting characteristics of silver phosphate, it was the subject of many studies for the photodegradation of dyes over thirteen year period from 2011 to 2023 (Fig. 1), owing to its forbidden band width. Furthermore, single Ag_3PO_4 [32] and its composites such as Ag_3PO_4/reduced graphene oxide/Bi_2MoO_6 [33], PANI/Ag_3PO_4/$NiFe_2O_4$ [34], and p-Ag_3PO_4/n-ZnO/C [35] proved an improved photocataltic activity. In adition to $Nd_2Sn_2O_7$/$Bi_2Sn_2O_7$/Ag_3PO_4 [36], Ag_3PO_4/Fe_3O_4/C_{60} [37], Ag_3PO_4/GO [38] and Ag_3PO_4/Polyndole [39] that could behave as well as potential candidates for antimicrobial applications thanks to their excellent activity against prevalent bacteria. On the other hand, it has been reported that the photocatalytic activity of silver phosphate with respect to dye photodegradation depends on many factors such as synthesis method, solution pH, dye concentration, and photocatalyst concentration [40]. These parameters have a significant effect on the morphology of Ag_3PO_4. Further thoughts, morphology has a closed relationship with the exposed facets of the crystals considered affecting the properties of catalysts. Studying Ag_3PO_4 with various nanostructures [37,38,39,40], depicted that rhombic dodecahedrons owned the elevated performance which was associated to the higher surface energy of {110} facets. Once the aqueous Ag_3PO_4 suspension is irradiated with photons energy greater than its band gap, the first step consists of the generation of (e^-/h^+) pair leading to the formation of strong oxidants, including hydroxyl radical and superoxide radical anion (eq (1)–(4).

$$Ag_3PO_4 + h\nu \rightarrow Ag_3PO_4 + h^+_{VB} + e^-_{CB} \quad (1)$$

$$Ag_3PO_4\left(h^+_{VB}\right) + OH^-_{ad} \rightarrow Ag_3PO_4 + OH^{\cdot} \quad (2)$$

$$Ag_3PO_4\left(h^+_{VB}\right) + H_2O \rightarrow Ag_3PO_4 + OH^{\cdot} + H^+ \quad (3)$$

$$Ag_3PO_4\left(e^-_{CB}\right) + O_2 \rightarrow Ag_3PO_4 + O_2^- \quad (4)$$

$$Pollutant + OH^{\cdot} \rightarrow oxidation\ products \quad (5)$$

$$Pollutant + h^+_{VB} \rightarrow oxidation\ products \quad (6)$$

$$Pollutant + e^-_{CB} \rightarrow reduction\ products \quad (7)$$

Table 1
Properties of Orange G dye.

Name	Orange G
Nature	Anionic dye
λ_{max} (nm)	478
Molecular weight (g/mol)	452.38
Molecular structure	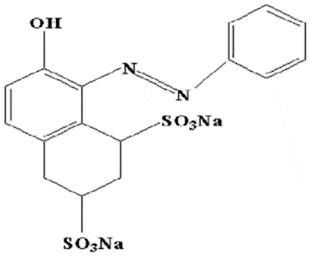

The interest in improving photocatalytic activity of silver phosphate by narrowing its band gap energy for instance, has driven to many studies on developing photocatalytic heterojunctions and doping [45]. Herein, it is worth mentioning that the synthesis method only can be sufficient and crucial to reduce this optical property.

The present study demonstrated an enhanced band gap energy of Ag_3PO_4 photocatalyst synthesized by a simple solid–solid method for the photodegradation of Orange G. In addition, response surface methodology (RSM) was used for the statistical design of experiments to discover the effect of some operational parameters on the removal efficiency including catalyst dose and pollutant concentration. Finally, a scavenger study was carried out to investigate the photoactive species involved in the photodegradation process, along with DFT calculations to predict the theoretical band gap energy of the silver phosphate photocatalyst.

2. Experimental

2.1. Chemicals

Silver nitrates $AgNO_3$ and diammonium hydrogen phosphate H$(NH_4)_2PO_4$ were purchased from Acros Corp (Belgium). Orange G ($C_{16}H_{10}N_2Na_2O_7S_2$) whose properties are given in Table 1., was obtained from Shanghai Aladdin Chemistry Corp (China).

2.2. Synthesis procedure

The photocatalyst concerned in this work which is Ag_3PO_4 has been fabricated through a simple synthesis method [46]. In a typical procedure as it is shown in Fig. 2, $AgNO_3$ (1.5 g) and $(NH_4)_2HPO_4$ (0.777 g) were subjected to grinding for 10 min until the mixture became a yellow powder. Therefore, the resulting muddy was put in a beaker and stirred magnetically in the presence of deionized water for ten minutes, and then gets centrifuged (3000 rpm, 15 min) to remove the impurities, followed by drying in the oven at 80 °C for 12 h. This operation was carried out twice to ensure a high purity of the synthesized photocatalyst.

2.3. Characterization techniques

The crystalline state of the obtained product was characterized by X-Ray diffraction (XRD) on a Rigaku Smart Lab SE X-ray diffractometer (XRD) in the 2θ range of 10-70° with CuKα radiation (λ = 1.5406 Å). The morphology and the size along with the elementary composition of the prepared product were verified using a field emission scanning electron microscope (JEOL JSM-6460LAV) from Japan and energy dispersive X-ray spectrometer (EDS) with X-ray photon energy of about 20 keV, respectively. Thermogravimetric analysis (TGA) was carried out TA

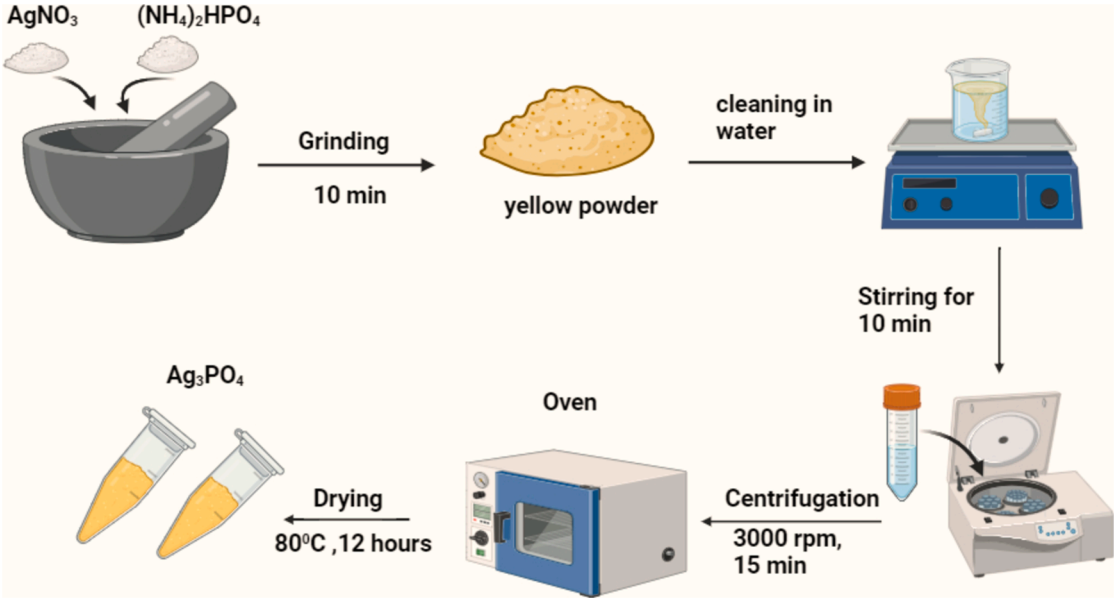

Fig. 2. Schematic diagram of ag_3PO_4 powder synthesis.

instrument, the sample powder was heated from room temperature to 600 °C under N_2 atmosphere. Fourier transform infrared (FTIR) spectra that was recorded in the Bruker instrument between 400 cm-1 to 4000 cm-1 to identify functional groups existed in the materials. UV − vis diffuse reflectance spectra (DRS) were recorded with a UV–Vis spectrophotometer (JASCO V-730) using $BaSO_4$ as the reference in the range of 250 to 850 nm. The absorbance of the samples was determined at 482 nm in a UV–Vis spectrophotometer (JENWAY 7205). The as prepared sample was also subjected to N_2 adsorption/desorption isotherms analysis (BET and BJH methods).

2.4. Photocatalytic tests

The photocatalytic activity of solid Ag_3PO_4 was evaluated by the photodegradation of Orange G under visible light irradiation. This procedure consists of mixing the chosen quantities of Orange G and Ag_3PO_4 photocatalyst, then the suspension was put in an ultrasonicator bath for 15 min to homogenize the solution. Thereafter, the suspension was placed in dark for 20 min to achieve adsorption–desorption equilibrium. A 250 W Xenon lamp was used as a source of visible light and the experiment was carried out under ambient atmospheric conditions. The suspension was taken out every four minutes and centrifuged (4000 rpm) to remove the photocatalyst particles then the absorbance was measured in a UV–Vis spectrophotometer.

2.5. Design of experiments

Getting some knowledge about a system to be studied allows us to achieve the high performance of an experimental design of this system. In this context, numerous factors can affect the photocatalytic degradation of hazardous materials such as dye concentration, catalyst amount, pH and reaction temperature [47]. The optimization is a perfect mathematical tool for adjusting variables in a process to discover the appropriate factors leading to the desired outcome [48]. It can be carried out using response surface methodology (RSM) and simplex optimization. In this work the photodegradation reaction was subjected to the response surface modeling (RSM) based on a central composite design (CCD), which is a frequent model used in environmental applications [49]. The number of total experiments (N) needed can be calculated by the equation $N = 2^k + 2*k + S$, where k corresponds to the number of factors, 2^k is the cubic runs coming from factorial design, 2*k and S are the axial runs and the number of central points respectively.

Table 2
Experimental Range and Levels of the Independent Test Variables.

Factors	Low (−1)	Middle (0)	High (+1)
Ag_3PO_4 (mg/L)	15	20	30
Orange G (mg/L)	10	15	20

Since the advanced oxidation processes aim to remediate wastewater by removing contaminants as dyes, the experimental measured response (Y) was the photodegradation percentage of Orange G. Two factors were considered: Ag_3PO_4 concentration (15–30 mg/L) and Orange G concentration (10–20 mg/L) as shown in Table 2..

The dye removal efficiency can be determined from equation (8), where C_o represents the initial concentration and C is the concentration at time t.

$$Y\% = \frac{C_o - C}{C_o} * 100 \quad (8)$$

The response surface analysis was performed using Minitab software version 21.1 to correlate the dependent and independent variables.

$$Y = \beta o + \sum_{i=1}^{2} \beta_i X_i + \sum_{i=1}^{2} \beta_{ii} X_i^2 + \sum_{i} \sum_{j=i+1} \beta_{ij} X_i X_j \quad (9)$$

Where Y is the predicted response; β_0 the constant coefficient; β_i the linear coefficients; β_{ii} the quadratic coefficients; β_{ij} is the interactive effects coefficient. X_i and X_j are independent factors.

2.6. Computational method

Through our study, all geometrical, electronic, and optical properties calculations were performed within the framework of Density Functional Theory (DFT) as part of the Vienna Ab Initio Simulation Package (VASP) [46,47,48]. The $(2s^2 2p^4)$-electrons in Oxygen, $(3s^2 3p^3)$-electrons in Phosphorus, and the $(4p^6 4d^{10} 5s^1)$-electrons in Silver were used as valence electrons, and the generalized gradient approximation in the form of Perdew Burke Ernzerhof (PBE) [53] functional was adopted self-consistently through the approach of the Projector Augmented Wave (PAW) [54] by Kohn − Sham electron wave functions expanded with an energy cutoff of 520 eV. The Monkhorst–Pack K-point [55] of 8 × 8 × 8

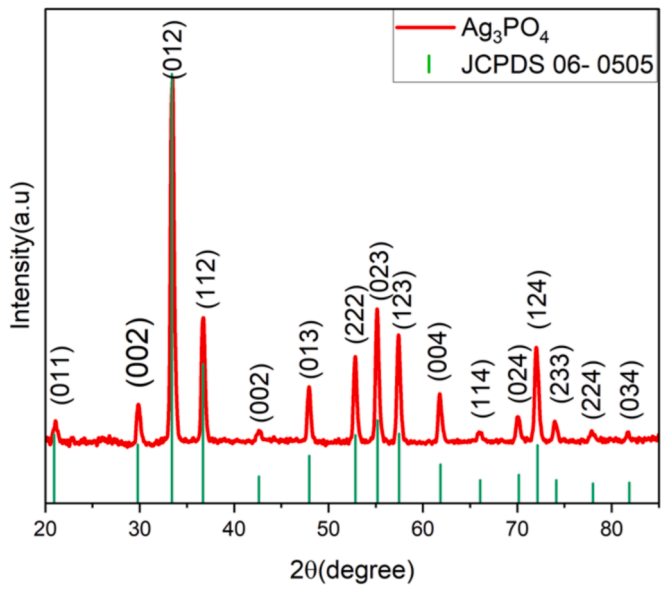

Fig. 3. X ray pattern of Ag_3PO_4.

and 16 × 16 × 16 grid were used respectively for structural and electronic properties of the Ag_3PO_4 bulk. For Ag_3PO_4 bulk full relaxation, all Ag-, P-, and O-atoms as well as lattice constants were permitted to be fully optimized using ISIF = 4. The contributions of dispersive interactions were taken into consideration by the DFT + D3 method [56]. The experimental value of the electronic band gap is often significantly underestimated when calculated using the standard GGA-PBE method. To address this, electronic properties were calculated using DFT augmented with the Hubbard U term (DFT + U approach). This adjustment particularly accounts for the correction of localized or strongly correlated electrons. In the context of the Simplified Local Density Approximation (LSDA) + U method, on-site Coulomb interaction terms have been incorporated for specific elements. These include a U-J term of 10.9300 for Oxygen (O) in the p orbital, and a U-J term of 16.01 for Silver (Ag) in the d orbital [57,58].

3. Results and discussion

3.1. XRD analysis

X-Ray Diffraction analysis was carried out to ensure an accurate synthesis of silver phosphate by achieving the phase structure and the purity of the material. According to the XRD measurement as shown in Fig. 3, Ag_3PO_4 was successfully synthesized and its crystal structure was compatible with the body-centered-cubic phase with the space group P-43n (JCPDS 06—0505) [31]. The characteristic peaks of Ag_3PO_4 powder at 21.1°, 29.9°, 33.3°, 36.8°, 42.7°, 48.0°, 52.9°, 55.2°, 57.3°, 61.8°, 66.1°, 70.1°, 72.1°, and 73.9° were indexed to the (011), (002), (012), (112), (002), (013), (222), (023), (123), (004), (114), (024), (124), and (233) diffraction planes, respectively [59]. The Rietveld refinement analysis was applied to enhance the understanding of the crystalline structure of the sample, confirming the successful synthesis of Ag_3PO_4 without the presence of any impurity phase. The profile refinement process utilized the Fullprof program software, employing the Pseudo-Voigt peak shape function. Multiple parameters were refined iteratively throughout the analysis, encompassing zero shifts, scale factors, background, lattice, line, atomic positional, and site occupations. The residual fitting intensity, as depicted by the line (Y_{Obs}-Y_{Cal}), displayed variations near zero on the intensity scale, indicating the high quality of the structural refinements (Fig. 4). The statistical parameters, including R_{wp}, R_p, and χ^2, exhibited relatively low values, underscoring the good agreement between the refined XRD pattern and the experimental data points (Table 3). Additionally, the refined lattice parameters and unit cell volumes are provided in Table for further insights into the structural

Table 3
Lattice parameter, unit cell volume and statistical parameters of quality obtained by rietveld refinement for ag_3PO_4.

R_p (%)	41.2
R_{wp} (%)	25.1
χ^2	1.94
a (Å)	6.012
V(Å^3)	217.3

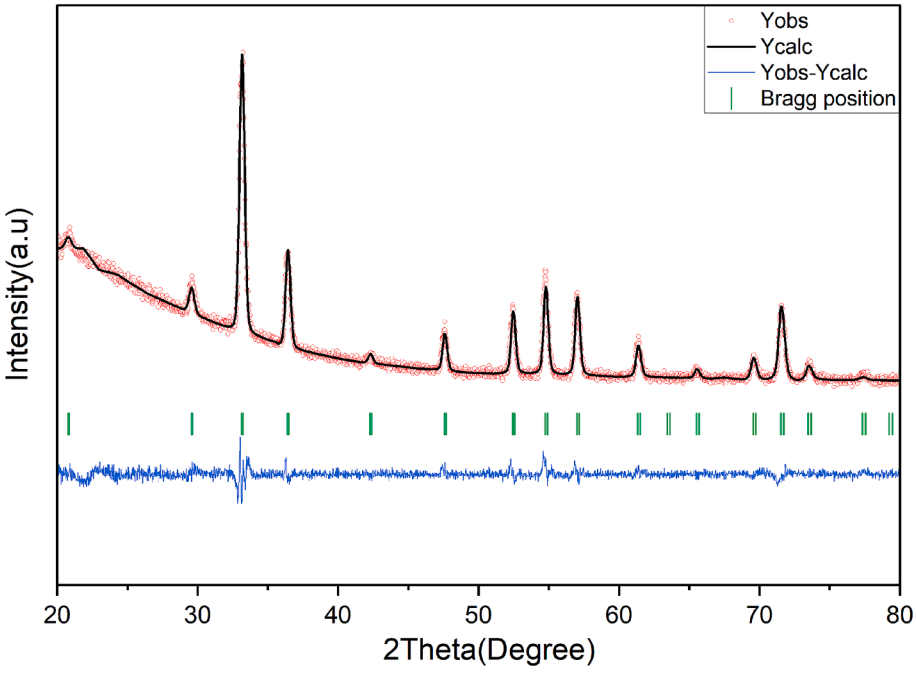

Fig. 4. Rietveld refinement of Ag_3PO_4 phase.

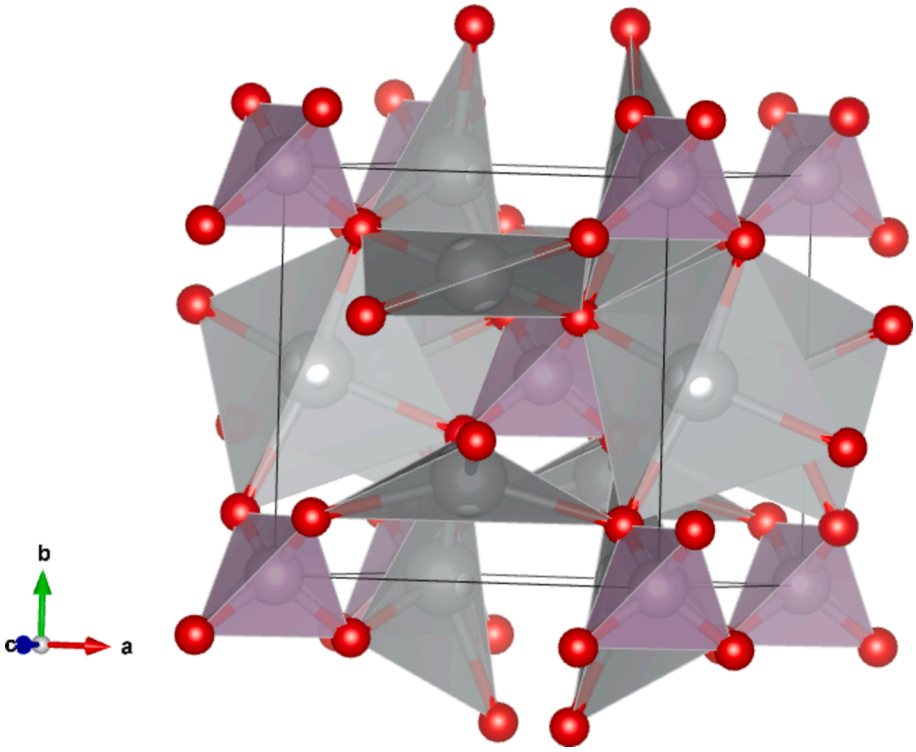

Fig. 5. Crystalline structure of Ag_3PO_4 with polyhedron.

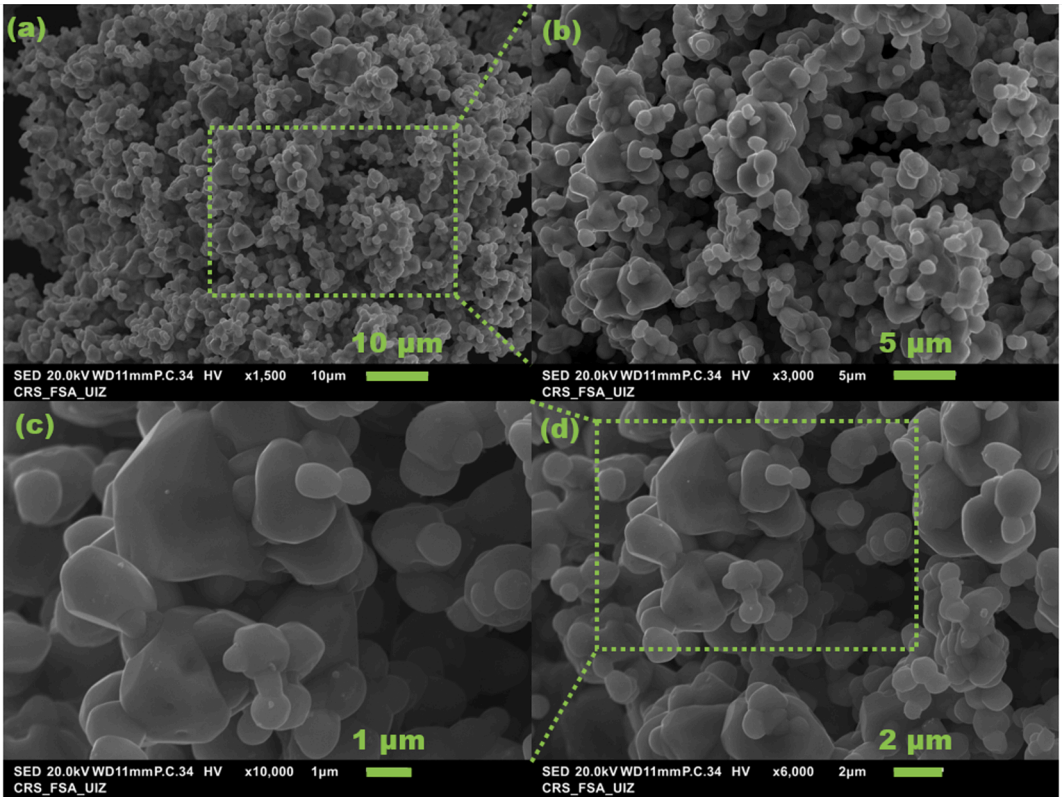

Fig. 6. SEM images of Ag_3PO_4 particles at different scales.

characteristics. A decrease in the cell volume and lattice parameters was observed compared to ICSD no. 1,400,030 [60]. This behavior is typically associated with the synthesis method, which introduces various types of structural defects, such as vacancies and local lattice disorders.

The modeling of the Ag_3PO_4 structure was conducted based on the Rietveld refinement results using the Visualization for Electronic and Structural Analysis (VESTA) **software (**Fig. 5**).** The Ag_3PO_4 phase consists of tetrahedral [PO_4] and [AgO_4] clusters. The [AgO_4] clusters

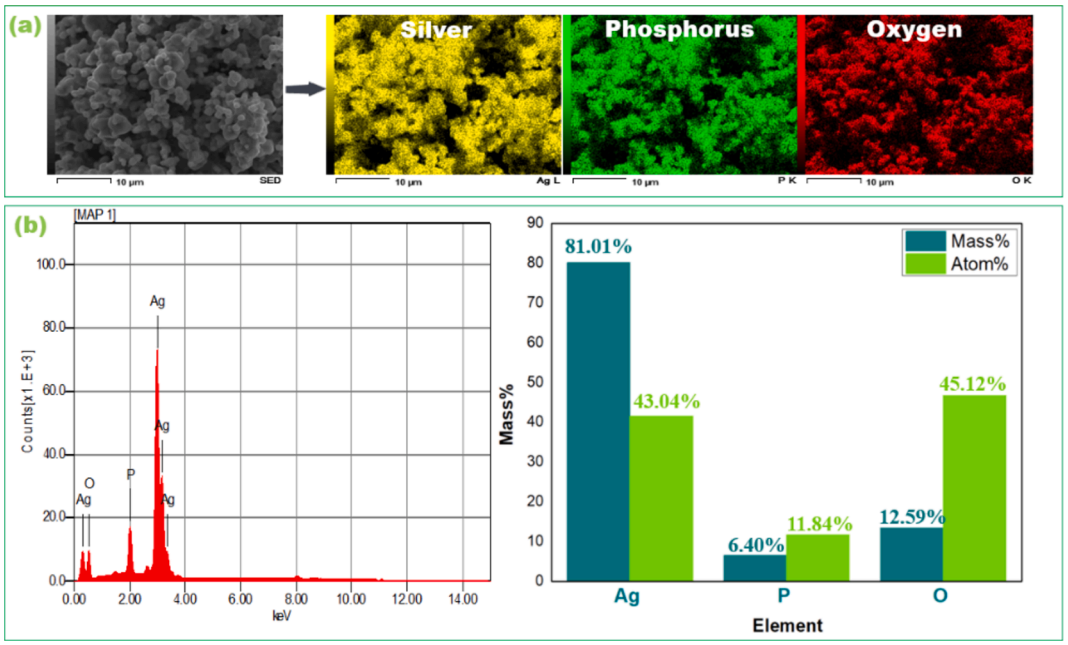

Fig. 7. EDS analysis of Ag_3PO_4 particles.

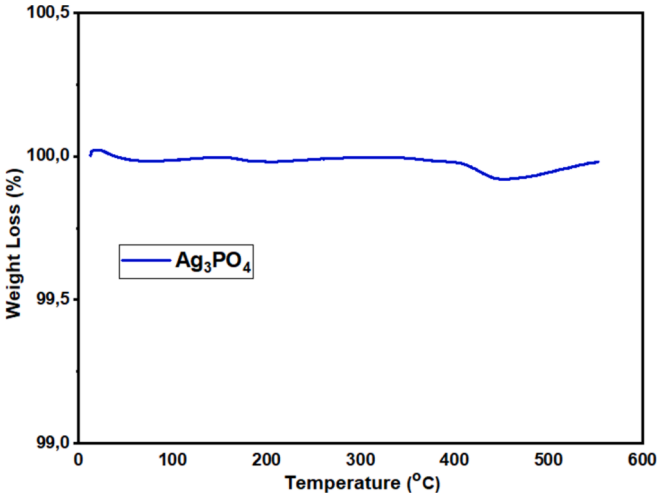

Fig. 8. TGA pattern of Ag_3PO_4.

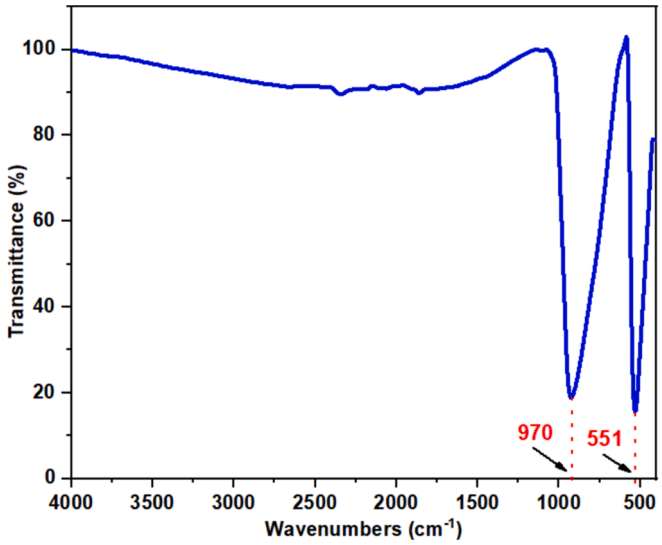

Fig. 9. FTIR spectrum of Ag_3PO_4 particles.

exhibit significant distortion, resulting in two types of O-Ag-O bonding angles.

3.2. SEM observations and EDX analysis

The additional morphologic characterization of the Ag_3PO_4 particles was investigated through SEM analysis. The results as shown in Fig. 6 indicate that Ag_3PO_4 particles synthesized by solid–solid route exhibit an irregular spherical shape with different particle size which is both the same and similar in a small portion to that obtained through precipitation [61–64] and hydrothermal [65] methods. In addition, though similar precursors used as for the as prepared Ag_3PO_4, the synthesis of Ag_3PO_4 particles by precipitation [66] reveals a cauliflower shape, indicating the direct effect of synthesis method on the morphology. EDX analysis was investigated as presented in Fig. 6, to further confirm the purity of the synthesized Ag_3PO_4. Assigned peaks of Ag, P and O atoms were detected without any impurity peaks. Thus, the synthesized photocatalyst is only composed of silver, phosphorus, and oxygen without other elements. According to the study by SEM-EDX mapping as shown in Fig. 7.**a,** the morphology of Ag_3PO_4 is well ordered and possesses a homogeneous distribution of particle size. The weight and atomic percentage of Ag, P and O are presented in the bar chart of Fig. 7.b. while the experimental weight percentages of Ag, P and O are 81.01 %, 6.40 % and 12.59 % respectively, the theoretical fractions were found to be 77.31 %, 7.39 % and 15.28 %. Hence, these close values prove the efficient yield of the synthesis method.

3.3. TGA analysis

The thermal stability of Ag_3PO_4 was examined by using thermogravimetric analysis under N_2 gas from 5°C to 800 °C. The TG curve as shown in Fig. 8, demonstrated that silver phosphate is thermally a durable material with a slight weight loss of 2 % up to 400 °C, depicting almost an identical thermal stability to the previous studies [63–66,69,70]. This characteristic proves the potency of Ag_3PO_4 for a

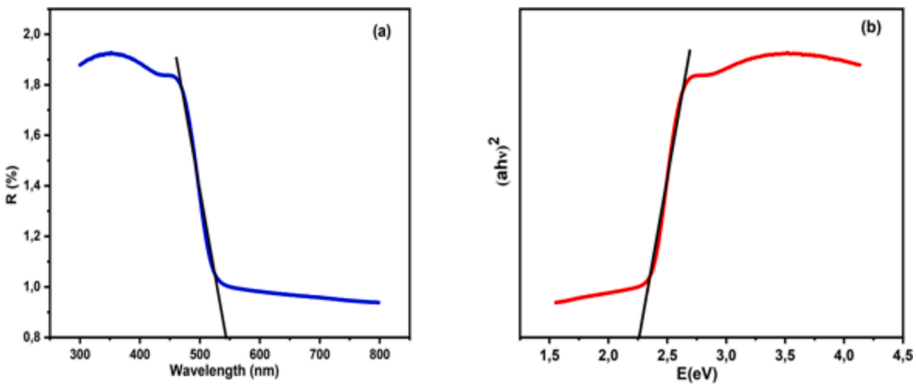

Fig. 10. Absorbance spectra (a) and Tauc plot (b) of Ag_3PO_4.

wide variety of other catalytic applications, including thermocatalysis, and photothermal catalysis.

3.4. ATR-FTIR spectroscopy

In order to get further information about both the nature and composition of the surface of synthesized Ag_3PO_4, Attenuated Total Reflection Fourier Transform Infrared (FTIR) spectroscopy was used. TheATR-FTIR spectra of raw Ag_3PO_4 which was recorded from 400 cm^{-1} to 4000 cm^{-1}as shown in Fig. 9, demonstrates the presence of two peaks at approximately 970 cm^{-1} and 551 cm^{-2} which are attributed to the stretching vibration modes of P-O band of PO_4, especially of the bulk Ag_3PO_4 as mentioned by Thomas et al [71]. According to the previous studies Ag_3PO_4, it can be concluded that Ag-O bond is not detectable by FT-IR analysis. However, using Raman spectroscopy as a complementary analysis revealed that the corresponding symmetrical vibration of the AgO bending bond is located at 113 cm^{-1} as mentioned by Abd El-Sattar and co-workers [72].

3.5. UV–vis diffuse reflectance spectroscopy (DRS)

Optical and electronic properties Ag_3PO_4 determined by using diffuse reflectance spectroscopy (DRS) [73]. In this work UV –vis-diffuse reflectance spectrum was collected on Jasco V-750 spectrophotometer where barium sulfate ($BaSO_4$) was used as a reference. Fig. 10 shows the UV − visible spectra of the solid Ag_3PO_4 photocatalyst. The band gap energy (E_{gap}) value was calculated using the Kubelka − Munk equation and Tauc method [74]. The silver phosphate sample depicted an E_g value of 2.25 eV which is roughly equivalent to a wavelength of 551 nm. Therefore, making indeed the as-prepared material a visible light active photocatalyst.

The valence band edge potential (EVB) and conduction band edge potential (ECB) of Ag_3PO_4 were calculated using Mulliken electrochemical equation [75].

$$x\left(A_aB_bC_c\right) = \left[x(A)^a.x(B)^b.x(C)^c\right]^{1/a+b+c} \tag{10}$$

$$E_{VB} = x - E_e + 0.5\,E_g \tag{11}$$

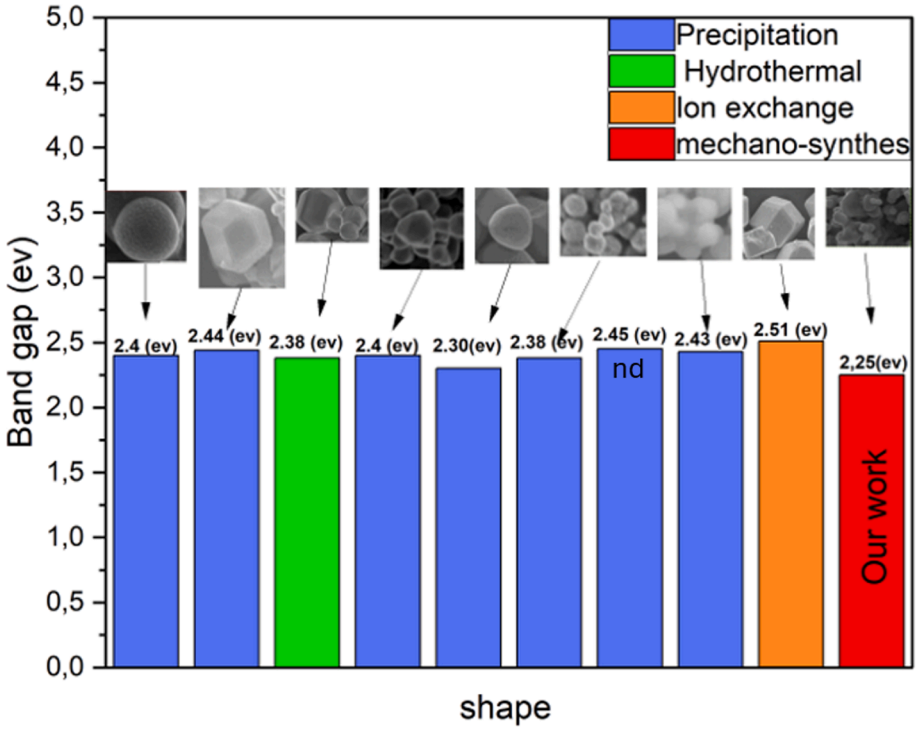

Fig. 11. Band gap of Ag_3PO_4 synthesized by different methods Vs. shapes [40–44,50–52,61–70,78,79].

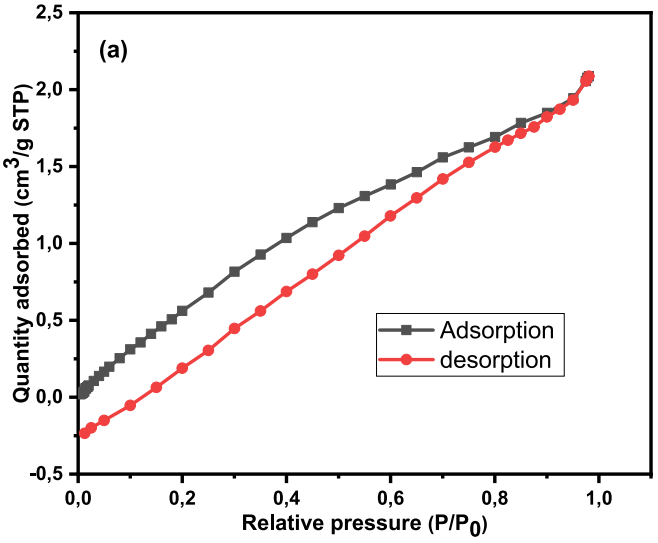

Fig. 12. Nitrogen sorption isotherm plot of Ag_3PO_4.

$$E_{CB} = x - E_e - 0.5E_g \quad (12)$$

where, E_e represents the energy of free electron on the hydrogen scale (≈ 4.5 eV/NHE), E_g is the energy of band gap, and x refers to the electronegativity of Ag_3PO_4 = 5.96 eV. The estimated ECB and EVB of Ag_3PO_4 are found to be 0.335 eV and 2.585 eV, respectively.

As shown in Fig. 11, most studies on Ag_3PO_4 photocatalyst synthesized by different wet methods, demonstrated that its band gap energy is about 2.30 to 2.51 eV. On the one hand, Ag_3PO_4 synthesized by different methods using the same precursors depicted approximately a closed Eg value (2.38–2.45 eV) with a particle size ranging from 200 nm to 500 nm, asserting the influence of synthesis method on the optical properties. On the other hand, the biggest particle size though solid Ag_3PO_4 has, its band gap (2.25 eV) is smaller than that of the other materials, which indicates that the particle size and band gap energy are reversely or normally proportional. This was proved before when Lin et al [76] synthesized TiO_2 for the photodegradation of 2-Chlorophenol. They discovered that while the particle size decreased, the band gap decreased as well. However, for ultra-fine TiO_2 particles the band gap increased. Depending on morphology, the lowest band gap energy was obtained with spherical and irregular spherical shapes. This factor has a significant impact on the optical properties of photocatalysts as it is mentioned by Suwanboon et al [77]. Briefly, considering hydrothermal, precipitation and ion exchange techniques, solid–solid method is another key strategy to decrease the band gap energy of silver phosphate.

3.6. BET surface area assessment

Nitrogen adsorption–desorption experiments were carried out to determine the pore size and structure of the silver phosphate. Specific surface area and porosity were determined using the Brunauer–Emmett–Teller (BET) and Barrett-Joyner-Halenda (BJH) method respectively. Fig. 12, illustrates an isotherm of Ag_3PO_4, which exhibits in the P/P0 range of 0–0.98. The desorption curve is nearly identical to the adsorption curve, with no discernible hysteresis loop, due to the minimal amount of N_2. Mainly, Ag_3PO_4 presents a similar type II adsorption isotherm.

The BET analysis report shows that silver phosphate possesses a decreased surface area of 3.84 m^2/g indicating a non-porous structure [80], along with a pore volume and diameter of 0.0032 cm^3/g and 1.01 nm respectively (Table 4).

S_{BET} BET surface area, V_P total pore volume, and D_P BJH adsorption average pore diameter.

Table 4
Textural properties of the Ag_3PO_4.

Sample	S_{BET} (m^2 g^{-1})	V_P (cm^3 g^{-1})	D_P (nm)
Ag_3PO_4	3.8400 m^2/g	0.0032	1.0100

3.7. Statistical analysis of Orange G degradation

Before the optimization, preliminary experiments were carried out to determine the effectiveness of the photocatalyst to remove Orange G from aqueous solution (Fig. 13). It was found that photodegradation efficiency could be achieved with 30 mg/L and 10 mg/L of catalyst and dye concentration respectively. The removal percentage of orange G attained 96 % after 20 min of irradiation and the photocatalytic degradation was proved to be a first order reaction. The rate constant was calculated from the **equation (13),** and it was found to be K = 0.1766 min^{-1}. Where [OG] is the concentration of orange G at time t and $[OG]_0$ consists of the initial concentration.

$$\ln\frac{[OG]}{[OG]o} = -kt \quad (13)$$

To identify the optimal values of both variables in relation to the photodegradation process, an experimental design was carried out considering the amounts of Ag_3PO_4 (15–30 mg/L) and Orange G (10–20 mg/L). It was concluded through RSM technique and based on desirability function, that the degradation of Orange G as shown in Fig. 16**.a** is promoted at 24.65 mg/L and 11.07 mg/L of Ag_3PO_4 and the pollutant successively (Table 6). Table 4 shows the real and recorded values. Most of the experiments showed a significant degradation (more than 80 %) in the presence of the photocatalyst. Based on these photodegradation results, the empirical relationship between the response (Y) and the two parameters which are catalyst dose (X1) and Orange G amount (X2) was obtained as shown in equation (14).

$$\boldsymbol{Y}(\%) = -\mathbf{15.5} + \mathbf{10.77}*\boldsymbol{X1} - \mathbf{1.975}*\boldsymbol{X1} - \mathbf{0.2102}\,\boldsymbol{X1}*\boldsymbol{X2} \quad (14)$$

ANOVA was used to evaluate the convenience and significance of the provided model, and the results are given in Table 5.**.** The quantitative correlation between experimental and predicted values can be evaluated by the square of determination coefficient, it was found to be 90.4 %, implying that 90.4 % of the variation can be explained considering X1 and X2 as model parameters. Another index of significance which is Fisher's F-value or the ratio between the mean square and residual error of the model is equal to 13.24, being larger than the critical point (2.36), which indicates that the model is a good predictor for the photodegradation of orange G. In the same context, the pareto chart demonstrates the effect of the parameters. As is clearly observed in Fig. 14, pollutant amount, photocatalyst concentration and its square are the most pre-eminent. Whereas concentrations interaction and the square of pollutant concentration are insignificant since their bars are below the reference line of response. Additionally, the 3D response surface plots and contour plots were plotted as shown in Fig. 15 **(a and b).** They illustrate the effects of silver phosphate and Orange G loading on the response (degradation efficiency). It can be observed that while the photocatalyst amount increases, degradation efficiency rises sharply. However, the greatest the pollutant concentration is, the lowest degradation efficiency is.

3.8. Photocatalytic evaluations

Given that semiconductors own a feeble adsorption capacity; that is to say, a short time is enough for the adsorption equilibrium, such as 30 min, 20 min and 10 min as chosen elsewhere [818283].Some tests were completed within 20 min under the optimal conditions, to evaluate the

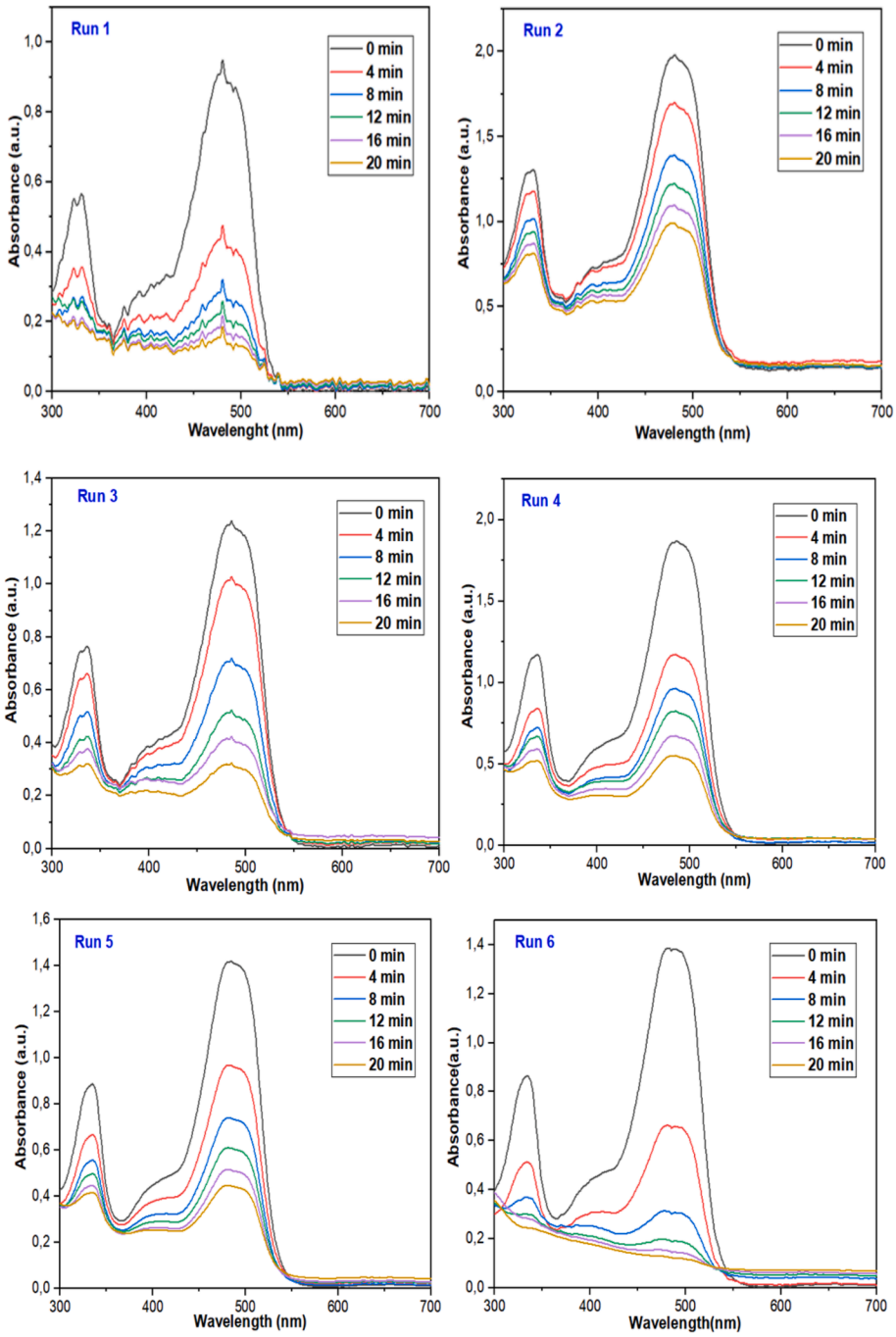

Fig. 13. Uv–Vis spectral analysis of the degradation of OG using Ag_3PO_4 with different concentrations.

photocatalytic activity of solid–solid Ag_3PO_4. The photodegradation profile of Orange G is given in Fig. 16**.a.** The curve demonstrates that when the mixture is exposed to darkness, the adsorption of orange G on Ag_3PO_4 surface rises slightly. Luo et al, illustrated that the adsorption of dye molecules including crystal violet (0.64 μmol/g) methylene blue (0.87 μmol/g) in comparison with Orange G (0.2 μmol/g) and methyl orange,is crucial for the photodegradation process [84]. This complication is ascribed to the interaction between an anionic dye (OG) and Ag_3PO_4 maintaining a negative charge [85]. During the irradiation in the presence of solid Ag_3PO_4 photocatalyst, the photodegradation efficiency reached about 93.02 % in a twenty-minute period under optimal conditions, which is in some extent consistent with the predicted removal efficiency (98.75 %). This prominent photocatalytic activity is further manifested by the absorption variation of Orange G characteristic band at 482 nm. Fig. 16**.a** shows that four minutes of irradiation were enough for a sharp decrease of the band intensity (about 50 % of degradation), then it almost disappeared after 20 min. Conversely; in previous studies where Ag_3PO_4 synthesized by precipitation was used as a photocatalyst, the removal efficiency of Orange G was declined with about 25 % and 80 % [84,86]. Thus, the photocatalytic activity of the solid synthesized Ag_3PO_4 contributed mainly to the removal of orange G instead of the adsorption as mentioned before.

From Table 7, it can be clearly observed that single Ag_3PO_4 depicted a remarkable photocatalytic activity for the photodegradation of Orange G in a short period in comparison with the other photocatalysts obtained by doping or by heterojunction construction. This demonstrated the

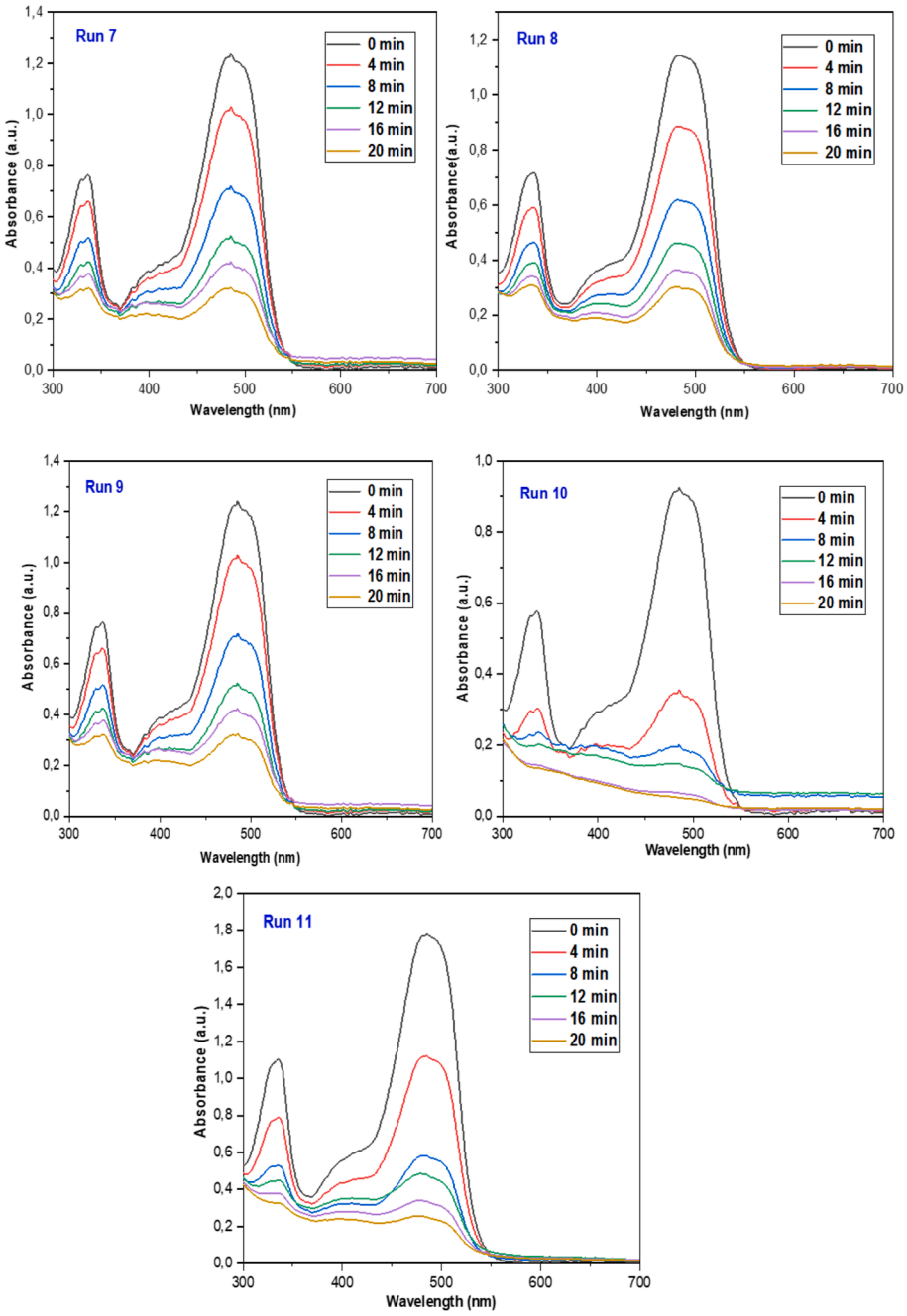

Fig. 13. (*continued*).

Table 5
Two-factor RSM-CCD matrix with response parameter

Runs	1	2	3	4	5	6	7	8	9	10	11
Photocatalyst (mg/L)	15	15	20	20	12.93	27.07	20	20	20	30	30
Orange G (mg/L)	10	20	7.93	22.07	15	15	15	15	15	10	20
Y_{exp}(%)	82.2	43.5	89.7	71.6	66.6	91.5	89.2	89.5	90.4	96	81.2
Y_{calc}(%)	79	59.2	91.3	72.2	58	92.3	86.1	86.1	86.1	98	78.8

ability to synthesize silver phosphate with respect to different materials obtained by desperate techniques leading to the high photocatalytic activity.

Understanding the interactions between photocatalysts and pollutants is important to describe the photodegradation mechanism. Responsible radicals of Orange G decomposition are determined thanks to a scavenger study using three photoactive species including isopropanol (IPA), Ethylenediaminetetraacetic acid disodium (EDTA) and

Table 6
Optimum values for optimal Orange G degradation.

Solution	Photocatalyst mg/l	Pollutant mg/l	Degradation fit %	Composite desirability
	24.6548	11.0722	98.7503	1

Ascorbic acid that reveal the generation of holes (h^+), peroxides radicals ($*O_2^-$) and hydroxyl radicals (*OH) respectively [87]. In this context, Fig. 17**.b** demonstrates that the photodegradation efficiency of Orange G over Ag_3PO_4 was approximately 72 % after 20 min. This slight decrease in the presence of isopropanol, indicates that the role of this scavenger was insignificant during the photodegradation mechanism. On the other hand, the removal percentage of Orange G was affected strongly by the addition of both EDTA and ascorbic acid with 5.61 % and 3.07 % consecutively. Thus, peroxides and hydroxyl radicals are paramount active species in the photodegradation of orange G in the presence of Ag_3PO_4. The proposal mechanism for this process is given in Fig. 18. When Ag_3PO_4 semiconductor is excited by solar radiation, an electron (e^-) from the valence band edge (EVB) moves to the conduction band edge (ECB), generating a hole (h^+) in the valence band (VB) and forming an electron-hole pair. The (e^- and h^+) pairs oxidize water molecules to hydroxyl radicals (*OH) using hole (h^+), and reduce the oxygen to the superoxide radicals ($*O_2^-$) through electron (e-). The generated radicals intervene in the photodegradation orange G molecules to H_2O and CO_2.

3.9. DFT calculations

We initially conducted an in-depth analysis of the geometrical structure of bulk Ag_3PO_4 compound. The full optimization based on the PBE-GGA yielded an equilibrium lattice parameter of 6.014 Å, aligning notably consistent with previously reported theoretical and experimental values. As illustrated in Fig. 19**.a,** the cubic structure of Ag_3PO_4 possesses a P-43n symmetry with a space group of 218, with each atom being tetrahedrally coordinated. Importantly, the presence of the $[PO4]^{3-}$ tetrahedron, which, due to its robust P–O bonds, tends to diminish the covalent aspect of the Ag–O bonds. This distinctive feature of the structure seems to be a key factor in hindering the hybridization between Ag's 4d and O's 2p orbitals. Consequently, this leads to the emergence of spatially extensive Ag s–Ag s hybrid bands at the conduction band minimum (CBM). Such a configuration of charge distribution at the CBM is indicative of a reduced effective mass for the photoexcited electrons, thereby facilitating efficient carrier transport to the surface.

Furthermore, to elucidate the electronic characteristic and the photogenerated charge migration mechanism within the bulk Ag_3PO_4

Analysis of Variance

Source	DF	Adj SS	Adj MS	F-Value	P-Value
Model	5	2220,15	444,03	13,24	0,002
Linear	2	1782,45	891,22	26,58	0,001
Photocatalyst mg/l	1	1023,81	1023,81	30,53	0,001
Pollutant mg/l	1	758,64	758,64	22,63	0,002
Square	2	633,02	316,51	9,44	0,010
Photocatalyst mg/l*Photocatalyst mg/l	1	421,57	421,57	12,57	0,009
Pollutant mg/l*Pollutant mg/l	1	172,71	172,71	5,15	0,058
2-Way Interaction	1	87,33	87,33	2,60	0,151
Photocatalyst mg/l*Pollutant mg/l	1	87,33	87,33	2,60	0,151
Error	7	234,72	33,53		
Lack-of-Fit	3	234,14	78,05	545,79	0,000
Pure Error	4	0,57	0,14		
Total	12	2454,87			

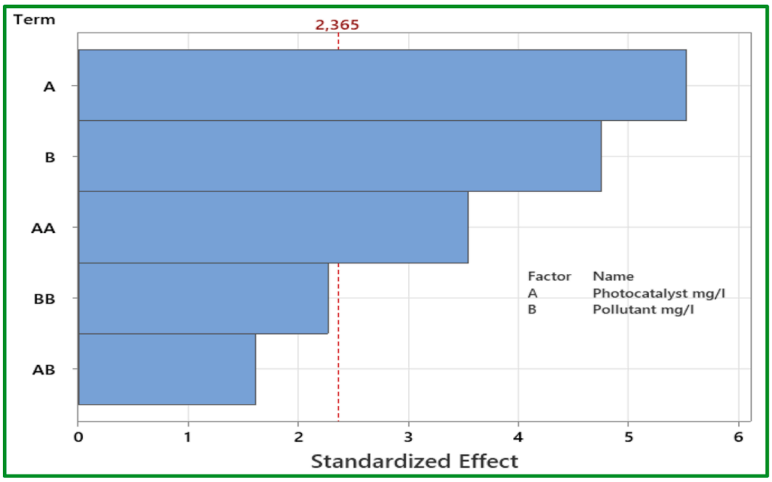

Fig. 14. Pareto chart for the photodegradation of Orange G.

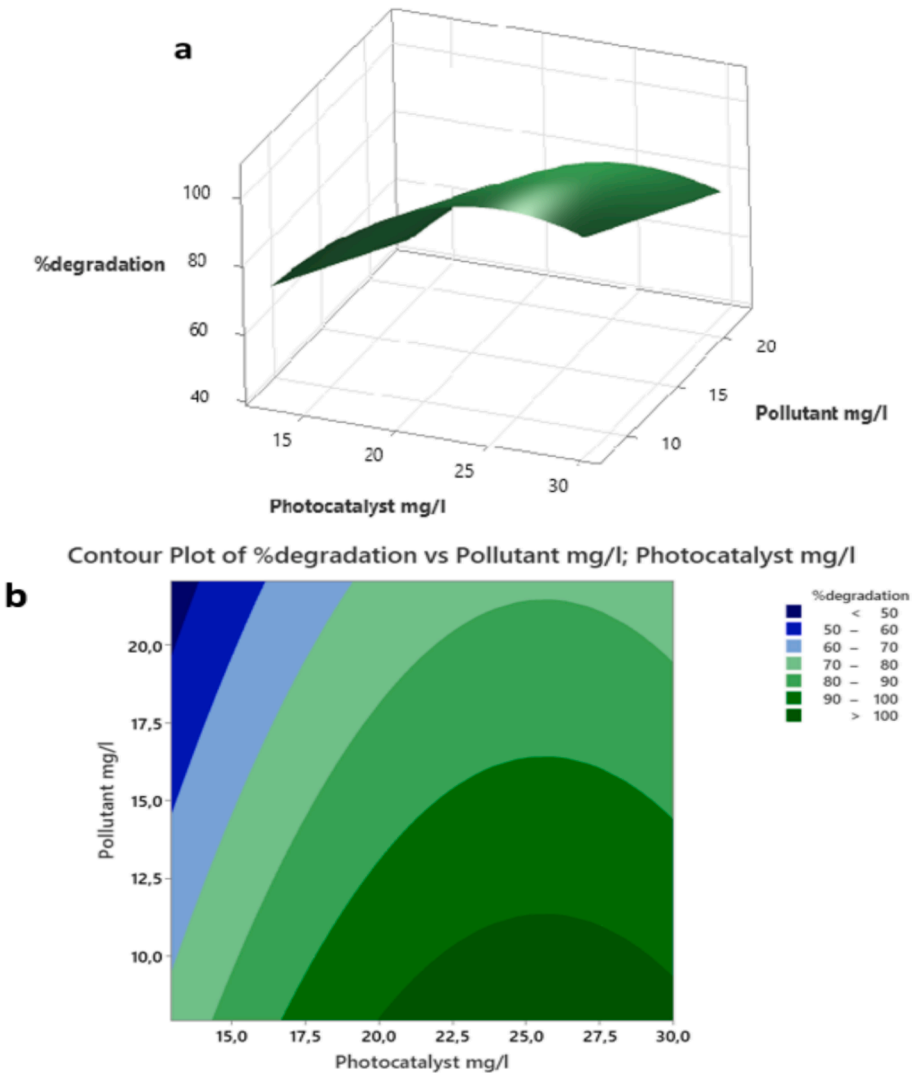

Fig. 15. (a) 3D response surface graph and (b) contour plot for Orange G degradation.

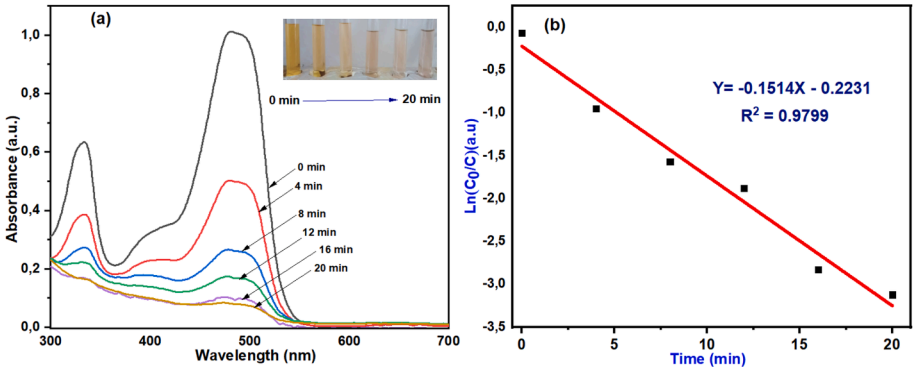

Fig. 16. (a) UV–Vis spectral of the degradation of OG by Ag_3PO_4 and (b) plots of (Ln (C_0/C)) versus irradiation time.

compound, extensive DFT calculations were conducted. Initially, the accuracy of the computational method used to determine electronic properties was assessed by calculating the band structure of bulk Ag_3PO_4 using various approaches. Fig. S1 illustrates the computed band structure using the GGA-PBE method. The computed band structure revealed an indirect bandgap of 0.16 eV, significantly underestimating the experimentally measured value of approximately 2.25 eV. Consequently, an alternative calculation approach was sought, leading to electronic property calculations employing the density-functional theory DFT + U approach. This approach yielded an indirect band gap of 2.19 eV for bulk Ag_3PO_4, occurring at the M (VBM) and Γ (CBM) points as depicted in Fig. 19**.b.** A notable characteristic of the electronic structure of bulk Ag_3PO_4 is its highly dispersive CBM, resulting in a small effective mass of photoexcited electrons. The CBM primarily comprises the delocalized 5 s orbitals of Ag atoms, facilitated by the formation of metallic Ag–Ag bonds that embrace the $[PO_4]^{3-}$ tetrahedral

Table 7
Comparison of Orange G (OG) degradation over Ag_3PO_4 with other photocatalysts.

Photocatalyst	Synthesis method	Bnad gap (eV)	Experimental conditions	Degradation	Refs
ZrO_2	precipitation	2.70	250 W Xenon lamp (λ = 365 nm). 100 mg of photocatalyst, 20 ppm OG	100 % in 180 min	[88]
B-TiO_2	Sol-gel	3	5 W UV light 0.5 g/L of photocatalyst, 10 mg/L OG.	97 % in 120 min	[89]
Mn-doped ZnO	chemical method.	2.60	30 mg/L of photocatalyst, 10 mg/L OG.	94 % in 60 min	[90]
ZnO/biomass activated carbon nanocomposite	hydrothermal	2.84	500 W tungsten lamp 1 g/L of photocatalyst, 50 mg/L OG.	70 % in 60 min	[91]
$ZnFe_2O_4$	reduction–oxidation	1.85	Xenon lamp 0.5 g/L of photocatalyst, 100 mg/L OG.	95 % in 60 min	[92]
Cu–Ni/TiO_2	coprecipitation	2.90	500 W halogen lamp. 1 g/L of photocatalyst, 50 mg/L OG.	54.9 % in 60 min	[93]
sepiolite-TiO_2 nanocomposites	microwave-hydrothermal	3.08	300 W Xe lamp. 0.8 g/L of photocatalyst, 10 mg/L OG.	98.8 % in 150 min	[94]
nitrogen-doped TiO_2	Calcination	2.8	500 W Xenon-arc lamp 1 g/L of photocatalyst, 25 mg/l OG	96.29 % in 150 min	[95]
WO_3/g-C_3N_4	Ultrasound assisated procedure	2.66	35 W Xe lamp. 0.2 g/L of photocatalyst, 20 mg/L OG.	97 % in 60 min	[96]
ZnO NPs/HS	Physical mixing	2.93	8 W Philip's lamp, 100 mg of photocatalyst, 50 mg/L OG	94.3 % in 120 min	[97]
Fe-MOF-NH_2	Solvothermal	2.69	300 W Xe lamp. 100 mg/L of photocatalyst, 50 mg/L OG.	100 % in 10 min	[98]
TiO_2	Gelation	3.04	125 W Philip's lamp. 25 mg of photocatalyst, 10^{-5} M OG.	100 % in 90 min	[99]
Ag_3PO_4	Solid-solid	2.25	250 W Xenon lamp 24.6 mg/L of photocatalyst, 11 mg/L OG.	93.02 % in 20 min	**This work**

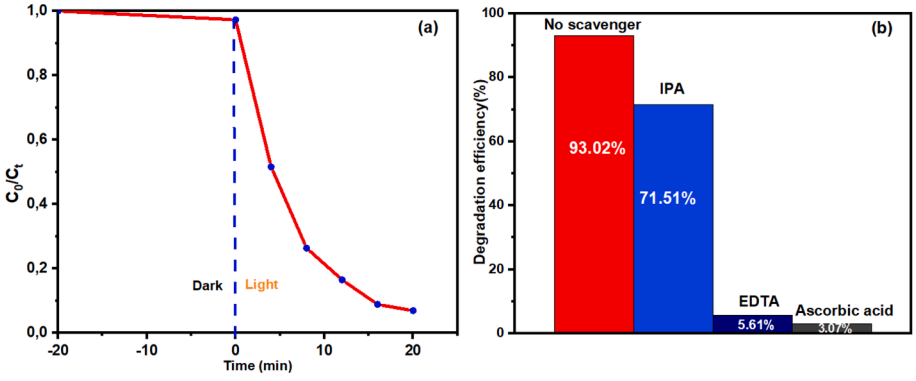

Fig. 17. (a) Profile of Orange G reduction and (b) trapping experiments of active species in the presence of Ag_3PO_4 under visible light.

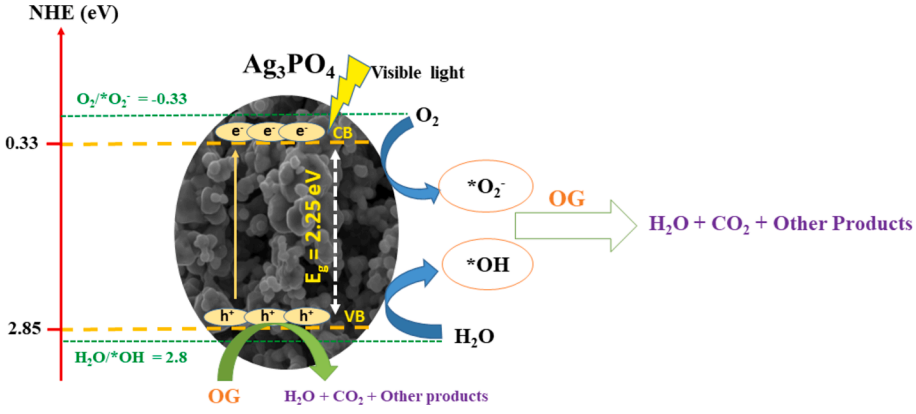

Fig. 18. The putative Photodegradation mechanism of Orange G on Ag_3PO_4.

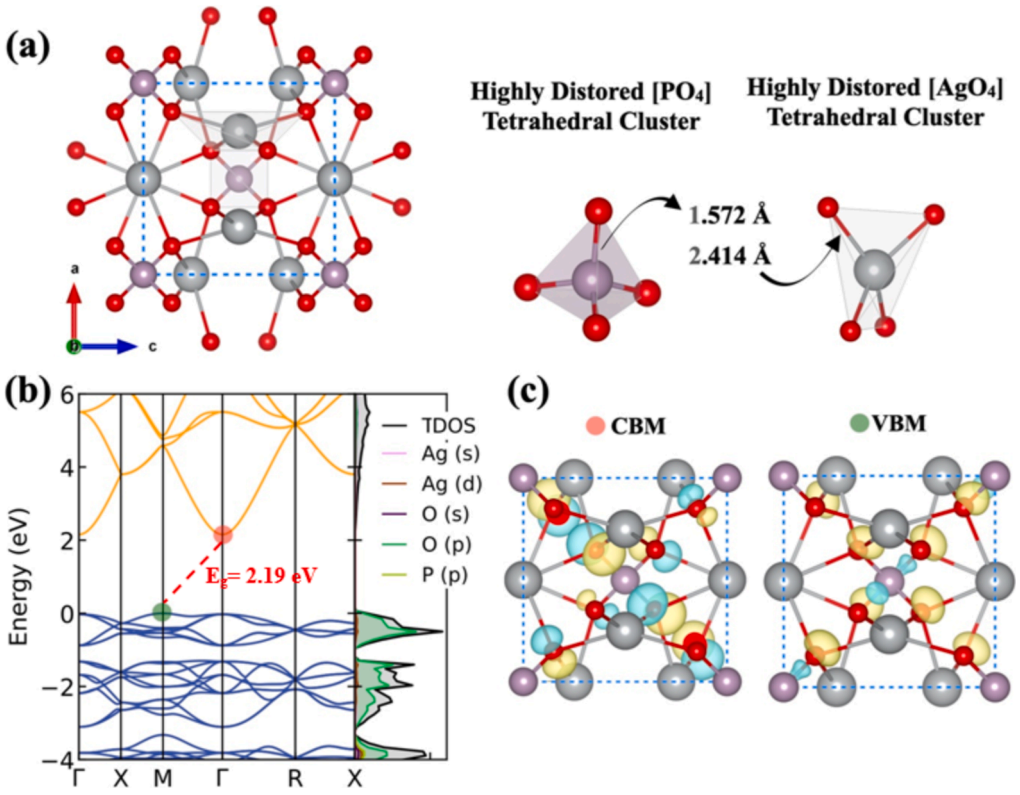

Fig. 19. DFT calculation results of bulk Ag_3PO_4. (a) Fully optimized unit-cell structure of cubic Ag_3PO_4, With a schematic illustration of the Tetrahedral [PO_4] and [AgO_4] clusters. Red, purple, and gray spheres represent Oxygen, Phosphorous, and Silver atoms, respectively. (b) Electronic Band structure with corresponding Total DOS (black line) and the PDOS (other colored lines). (c) Isosurfaces of the band-decomposed partial charge density of the valence band maximum (VBM) and conduction band minimum (CBM).

units, thereby enhancing the transfer of photoexcited electrons. Conversely, the VBM is predominantly characterized by O 2p and Ag 4d orbitals, with relatively flat energy bands near the VBM contributing to a large effective mass of photoexcited holes. Further insight into the characteristics of the band edges is provided through the band-decomposed partial charge density for the VBM and CBM as illustrated in Fig. 19**.c.** Notably, these plots demonstrate that the VBM primarily consists of states from P and O atoms, with the P-O plane facilitating a dense route for charge conduction.

4. Conclusion

In summary, we have reported the synthesis of Ag_3PO_4 by mechanosynthesis. The characterization of the prepared Ag_3PO_4 material revealed its purity and its stability, what opens the door to multiple future studies for different thermal applications. Indeed, this study emphasizes the promoted band gap energy of silver phosphate (2.25 eV) by virtue of the synthesis method. This statement was supported by DFT calculations confirming the approximate optical property. Furthermore, the photocatalytic activity of Ag_3PO_4 was evaluated through the photodegradation of orange G under visible light and the experiments proved the efficient removal of the dye pollutant under visible light irradiation.

CRediT authorship contribution statement

Ali Ait Baha: Writing – original draft, Data curation, Conceptualization. **Nabil Khosossi:** Software, Data curation. **Omar Lakbita:** Writing – review & editing, Validation, Resources, Data curation. **Younes Brahmi:** Writing – review & editing, Software, Data curation, Conceptualization. **Yassine El Mernissi:** Investigation, Data curation. **Taoufyq Aziz:** Validation, Supervision. **Abdeljalil Benlhachemi:** Writing – review & editing, Validation. **Bahcine Bakiz:** Validation. **Hicham Abou Oualid:** Supervision, Methodology, Investigation, Conceptualization.

Funding

This work was achieved thanks to the financial support of Green Energy Park (IRESEN-UM6P) internships, in addition to the joint efforts from the Faculty of Sciences of Agadir.

Declaration of competing interest

The authors declare the following financial interests/personal relationships which may be considered as potential competing interests: HICHAM ABOU OUALID reports administrative support, equipment, drugs, or supplies, and writing assistance were provided by Green Energy Park. HICHAM ABOU OUALID reports a relationship with Green Energy Park that includes: employment. If there are other authors, they declare that they have no known competing financial interests or personal relationships that could have appeared to influence the work reported in this paper.

Acknowledgments

The authors gratefully acknowledge Green Energy Park for the internship program and Ibn Zohr University for logistical support. Dr. Soukaina Hrifech and Dr. Oussama Oulhakem are also acknowledged for their assistance in the thermal energy storage laboratory and thin films laboratory at the Green Energy Park platform.

Appendix A. Supplementary material

Supplementary data to this article can be found online at https://doi.org/10.1016/j.cplett.2024.141681.

Data availability

Data will be made available on request.

References

[1] S. Gottardo *et al.*, "Towards safe and sustainable innovation in nanotechnology: State-of-play for smart nanomaterials," *NanoImpact*, vol. 21, no. January, 2021, doi: 10.1016/j.impact.2021.100297.

[2] Y. Wu *et al.*, "Bioenergy production and environmental impacts," *Geosci. Lett.*, vol. 5, no. 1, 2018, doi: 10.1186/s40562-018-0114-y.

[3] D. Fatta-Kassinos, S. Meric, A. Nikolaou, Pharmaceutical residues in environmental waters and wastewater: Current state of knowledge and future research, Anal. Bioanal. Chem. 399 (1) (2011) 251–275, https://doi.org/10.1007/s00216-010-4300-9.

[4] A. Nezamzadeh-Ejhieh, M. Kabiri-Samani, Effective removal of Ni(II) from aqueous solutions by modification of nano particles of clinoptilolite with dimethylglyoxime, J. Hazard. Mater. 260 (2013) 339–349, https://doi.org/10.1016/j.jhazmat.2013.05.014.

[5] J. Wang, H. Chen, Catalytic ozonation for water and wastewater treatment: Recent advances and perspective, Sci. Total Environ. 704 (2020) 135249, https://doi.org/10.1016/j.scitotenv.2019.135249.

[6] M. Hu, Y. Liu, Z. Yao, L. Ma, X. Wang, Catalytic reduction for water treatment, Front. Environ. Sci. Eng. 12 (1) (2018) 1–18, https://doi.org/10.1007/s11783-017-0972-0.

[7] G.L. Dotto, G. McKay, Current scenario and challenges in adsorption for water treatment, J. Environ. Chem. Eng. 8 (4) (2020) 103988, https://doi.org/10.1016/j.jece.2020.103988.

[8] J.Q. Jiang, The role of coagulation in water treatment, Curr. Opin. Chem. Eng. 8 (2015) 36–44, https://doi.org/10.1016/j.coche.2015.01.008.

[9] M. Gavrilescu, M. Macoveanu, Process engineering in biological aerobic wastewater treatment, Acta Biotechnol. 19 (2) (1999) 111–145, https://doi.org/10.1002/abio.370190205.

[10] H.T. Madsen, Membrane Filtration in Water Treatment - Removal of Micropollutants. (2014), https://doi.org/10.1016/B978-0-444-53178-0.00006-7.

[11] S. Hube, et al., Direct membrane filtration for wastewater treatment and resource recovery: A review, Sci. Total Environ. 710 (2020), https://doi.org/10.1016/j.scitotenv.2019.136375.

[12] M. Saeed, M. Muneer, A. ul Haq, N. Akram, Photocatalysis: an effective tool for photodegradation of dyes—a review, Environ. Sci. Pollut. Res. 29 (1) (2022) 293–311, https://doi.org/10.1007/s11356-021-16389-7.

[13] A. Houas, H. Lachheb, M. Ksibi, E. Elaloui, C. Guillard, J.M. Herrmann, Photocatalytic degradation pathway of methylene blue in water, Appl. Catal. B Environ. 31 (2) (2001) 145–157, https://doi.org/10.1016/S0926-3373(00)00276-9.

[14] J.-M. HERRMANN, "Water Treatment By Heterogeneous Photocatalysis," pp. 171–194, 1999, doi: 10.1142/9781848160613_0009.

[15] S. Li, et al., Photocatalytic degradation of hazardous organic pollutants in water by Fe-MOFs and their composites: A review, J. Environ. Chem. Eng. 9 (5) (2021) 105967, https://doi.org/10.1016/j.jece.2021.105967.

[16] S. Ahmed, M.G. Rasul, W.N. Martens, R. Brown, M.A. Hashib, Heterogeneous photocatalytic degradation of phenols in wastewater: A review on current status and developments, Desalination 261 (1–2) (2010) 3–18, https://doi.org/10.1016/j.desal.2010.04.062.

[17] N. Puri and A. Gupta, "Water remediation using titanium and zinc oxide nanomaterials through disinfection and photo catalysis process: A review," *Environ. Res.*, vol. 227, no. March, p. 115786, 2023, doi: 10.1016/j.envres.2023.115786.

[18] S. Gao, et al., Photocatalytic Removal of Tetrabromobisphenol A by Magnetically Separable Flower-like BiOBr/BiOI/Fe3O4 Hybrid Nanocomposites under Visible-Light Irradiation vol. 331 (2017), https://doi.org/10.1016/j.jhazmat.2017.02.030.

[19] J. Kim, J. Kim, Arsenite oxidation-enhanced photocatalytic degradation of phenolic pollutants on platinized TiO2, Environ. Sci. Technol. 48 (22) (2014) 13384–13391, https://doi.org/10.1021/es504082r.

[20] C. F. Cf, "MOLECULAR Electrochemical Photolysis of Water at a Semiconductor Electrode One and Two-dimensional Structure of Alpha-Helix and Beta-Sheet Forms of Poly (L-Alanine) shown by Specific Heat Measurements at Low Temperatures (1 . 5-20 K)," vol. 238, pp. 37–38, 1972.

[21] B. Bakbolat, et al., Recent developments of TiO2-based photocatalysis in the hydrogen evolution and photodegradation: A review, Nanomaterials 10 (9) (2020) 1–16, https://doi.org/10.3390/nano10091790.

[22] H. Huang, G. Chen, Y. Zhang, Two Bi-based phosphate photocatalysts: Crystal structure, optical property and photocatalytic activity, Inorg. Chem. Commun. 44 (2014) 46–49, https://doi.org/10.1016/j.inoche.2014.02.047.

[23] M.H. Fulekar, A. Singh, D.P. Dutta, M. Roy, A. Ballal, A.K. Tyagi, Ag incorporated nano BiPO4: Sonochemical synthesis, characterization and improved visible light photocatalytic properties, RSC Adv. 4 (20) (2014) 10097–10107, https://doi.org/10.1039/c3ra44488k.

[24] T. Yan, W. Guan, L. Cui, Y. Xu, J. Tian, Immobilization of cadmium ions to synthesis hierarchical flowerlike cadmium phosphates microspheres and their application in the degradation of organic pollutants under light irradiation, RSC Adv. 5 (54) (2015) 43756–43764, https://doi.org/10.1039/c5ra07224g.

[25] C. Zhang, et al., Cu2(OH)PO4/reduced graphene oxide nanocomposites for enhanced photocatalytic degradation of 2,4-dichlorophenol under infrared light irradiation, RSC Adv. 8 (7) (2018) 3611–3618, https://doi.org/10.1039/c7ra12684k.

[26] X. Li, X. Xiao, Q. Li, J. Wei, H. Xue, H. Pang, Metal (M = Co, Ni) phosphate based materials for high-performance supercapacitors, Inorg. Chem. Front. 5 (1) (2018) 11–28, https://doi.org/10.1039/c7qi00434f.

[27] R. Guo, et al., Phosphate-Based Electrocatalysts for Water Splitting: Recent Progress, ChemElectroChem 5 (24) (2018) 3822–3834, https://doi.org/10.1002/celc.201800996.

[28] A. Redinger, S. Siebentritt, "Loss Mechanisms in Kesterite Solar Cells", *Copp*, Zinc Tin Sulfide-Based Thin-Film Sol. Cells 627 (2015) 363–386, https://doi.org/10.1002/9781118437865.ch16.

[29] Z. Yi, et al., An orthophosphate semiconductor with photooxidation properties under visible-light irradiation, Nat. Mater. 9 (7) (2010) 559–564, https://doi.org/10.1038/nmat2780.

[30] J.J. Liu, X.L. Fu, S.F. Chen, Y.F. Zhu, Electronic structure and optical properties of Ag3PO4 photocatalyst calculated by hybrid density functional method, Appl. Phys. Lett. 99 (19) (2011) 2011–2014, https://doi.org/10.1063/1.3660319.

[31] R. Ng, H.N; Calvo, C; Faggiani, "A new investigation of the structure of silver orthophosphate".

[32] Y. Zhang, X. Zhang, R. Hu, Y. Yang, P. Li, Q. Wu, Bifunctional nano-Ag3PO4 with capabilities of enhancing ceftazidime for sterilization and removing residues, RSC Adv. 9 (31) (2019) 17913–17920, https://doi.org/10.1039/c9ra01969c.

[33] P. Zhu, Y. Chen, M. Duan, Z. Ren, M. Hu, Construction and mechanism of a highly efficient and stable Z-scheme Ag3PO4/reduced graphene oxide/Bi2MoO6 visible-light photocatalyst, Catal. Sci. Technol. 8 (15) (2018) 3818–3832, https://doi.org/10.1039/c8cy01087k.

[34] Y. Chen, P. Zhu, M. Duan, J. Li, Z. Ren, P. Wang, Fabrication of a magnetically separable and dual Z-scheme PANI/Ag3PO4/NiFe2O4 composite with enhanced visible-light photocatalytic activity for organic pollutant elimination, Appl. Surf. Sci. 486 (May) (2019) 198–211, https://doi.org/10.1016/j.apsusc.2019.04.232.

[35] M. Hu, P. Zhu, M. Liu, J. Xu, M. Duan, J. Lin, Preparation, performance and mechanism of p-Ag3PO4/n-ZnO/C heterojunction with IRMOF-3 as precursor for efficient photodegradation of norfloxacin, Colloids Surfaces A Physicochem. Eng. Asp. vol. 628, no. July (2021) 127235, https://doi.org/10.1016/j.colsurfa.2021.127235.

[36] P. Zhu, et al., Nd2Sn2O7/Bi2Sn2O7/Ag3PO4 double Z-type heterojunction for antibiotic photodegradation under visible light irradiation: Mechanism, optimization and pathways, Sep. Purif. Technol. vol. 300, no. August (2022) 121897, https://doi.org/10.1016/j.seppur.2022.121897.

[37] S. Sepahvand, S. Farhadi, Fullerene-modified magnetic silver phosphate (Ag3PO4/Fe3O4/C60) nanocomposites: Hydrothermal synthesis, characterization and study of photocatalytic, catalytic and antibacterial activities, RSC Adv. 8 (18) (2018) 10124–10140, https://doi.org/10.1039/c8ra00069g.

[38] B. Ji, W. Zhao, J. Duan, L. Fu, L. Ma, Z. Yang, Immobilized Ag3PO4/GO on 3D nickel foam and its photocatalytic degradation of norfloxacin antibiotic under visible light, RSC Adv. 10 (8) (2020) 4427–4435, https://doi.org/10.1039/c9ra08678a.

[39] S. Podder, et al., Bioactive silver phosphate/polyindole nanocomposites, RSC Adv. 10 (19) (2020) 11060–11073, https://doi.org/10.1039/d0ra01129k.

[40] C. Zhu, Y. Li, Y. Yang, Y. Chen, Z. Yang, P. Wang, Influence of operational parameters on photocatalytic decolorization of a cationic azo dye under visible-light in aqueous Ag 3 PO 4, Inorg. Chem. Commun. vol. 115, no. February (2020) 107850, https://doi.org/10.1016/j.inoche.2020.107850.

[41] Y. Bi, S. Ouyang, N. Umezawa, J. Cao, and J. Ye, "[emuch.net]AgPO4晶面控制FacetEffectofSingle-CrystallineAg3PO4Sub-microcrystalsonPhotocatalyticProperties.pdf," *J. Am. Chem. Soc.*, vol. 4, no. 06, pp. 6490–6492, 2011, [Online]. Available: https://doi.org/10.1021/ja2002132.

[42] Z. Jiao, Y. Zhang, H. Yu, G. Lu, J. Ye, Y. Bi, Concave trisoctahedral Ag3PO4 microcrystals with high-index facets and enhanced photocatalytic properties, Chem. Commun. 49 (6) (2013) 636–638, https://doi.org/10.1039/c2cc37324f.

[43] Y. Bi, H. Hu, S. Ouyang, Z. Jiao, G. Lu, J. Ye, Selective growth of metallic Ag nanocrystals on Ag 3PO 4 submicro-cubes for photocatalytic applications, Chem. - A Eur. J. 18 (45) (2012) 14272–14275, https://doi.org/10.1002/chem.201201435.

[44] J. Wang, F. Teng, M. Chen, J. Xu, Y. Song, X. Zhou, Facile synthesis of novel Ag3PO4 tetrapods and the 110 facets-dominated photocatalytic activity, CrystEngComm 15 (1) (2013) 39–42, https://doi.org/10.1039/c2ce26060c.

[45] G. Liu, L. Wang, H.G. Yang, H.M. Cheng, G.Q. Lu, Titania-based photocatalysts - Crystal growth, doping and heterostructuring, J. Mater. Chem. 20 (5) (2010) 831–843, https://doi.org/10.1039/b909930a.

[46] A. El Yacoubi, A. Rezzouk, B. Sallek, B.c. El Idrissi, "effect of Synthesis Method on Photocatalytic Activity of Ag 3 PO 4 Evaluated by ! Different Dyes L =" 2508 (2017) 4866–4871.

[47] A. Kumar, A Review on the Factors Affecting the Photocatalytic Degradation of Hazardous Materials, Mater. Sci. Eng. Int. J. 1 (3) (2017) 106–114, https://doi.org/10.15406/mseij.2017.01.00018.

[48] R.A. Olivero, J.M. Nocerino, S.N. Deming, Experimental Design and Optimization, Handb. Environ. Chem. 2 (1995) 73–122, https://doi.org/10.1007/978-3-540-49148-4_3.

[49] M. Shoorangiz, M.R. Nikoo, M. Salari, G.R. Rakhshandehroo, M. Sadegh, Optimized electro-Fenton process with sacrificial stainless steel anode for degradation/mineralization of ciprofloxacin, Process Saf. Environ. Prot. 132 (2019) 340–350, https://doi.org/10.1016/j.psep.2019.10.011.

[50] G. Kresse, J. Hafner, Ab initio molecular dynamics for open-shell transition metals, Phys. Rev. B 48 (17) (1993) 13115–13118, https://doi.org/10.1103/PhysRevB.48.13115.

[51] G. Kresse, J. Furthmüller, Efficiency of ab-initio total energy calculations for metals and semiconductors using a plane-wave basis set, Comput. Mater. Sci. 6 (1) (1996) 15–50, https://doi.org/10.1016/0927-0256(96)00008-0.

[52] G. Kresse, J. Furthmüller, Efficient iterative schemes for ab initio total-energy calculations using a plane-wave basis set, Phys. Rev. B - Condens. Matter Mater. Phys. 54 (16) (1996) 11169–11186, https://doi.org/10.1103/PhysRevB.54.11169.

[53] J.P. Perdew, K. Burke, M. Ernzerhof, Generalized gradient approximation made simple, Phys. Rev. Lett. 77 (18) (1996) 3865–3868, https://doi.org/10.1103/PhysRevLett.77.3865.

[54] P.E. Blöchl, Projector augmented-wave method, Phys. Rev. B 50 (24) (1994) 17953–17979, https://doi.org/10.1103/PhysRevB.50.17953.

[55] M. Methfessel, A.T. Paxton, High-precision sampling for Brillouin-zone integration in metals, Phys. Rev. B 40 (6) (1989) 3616–3621, https://doi.org/10.1103/PhysRevB.40.3616.

[56] A. Allouche, Software News and Updates Gabedit — A Graphical User Interface for Computational Chemistry Softwares, J. Comput. Chem. 32 (2012) 174–182, https://doi.org/10.1002/jcc.

[57] C. Zheng, H. Yang, Y. Yang, Pseudocapacitive behavior of Ag3PO4 nanospheres prepared by a sonochemical process, Mater. Trans. 58 (2) (2017) 298–301, https://doi.org/10.2320/matertrans.M2016312.

[58] F. Paquin, J. Rivnay, A. Salleo, N. Stingelin, C. Silva, Multi-phase semicrystalline microstructures drive exciton dissociation in neat plastic semiconductors, J. Mater. Chem. C 3 (207890) (2015) 10715–10722, https://doi.org/10.1039/b000000x.

[59] L. Liu, et al., A stable Ag3PO4@g-C3N4 hybrid core@shell composite with enhanced visible light photocatalytic degradation, Appl. Catal. B Environ. 183 (2016) 133–141, https://doi.org/10.1016/j.apcatb.2015.10.035.

[60] P.R. Masse, I. Tordjman, A. Durif, Affinement de la structure cristalline du monophosphate d'argent Ag3PO4. Existence d'une forme haute témperaturc, Zeitschrift Fur Krist. - New Cryst. Struct. 144 (1–6) (1976) 76–81, https://doi.org/10.1524/zkri.1976.144.1-6.76.

[61] S. Thiyagarajan, S. Singh, D. Bahadur, Reusable sunlight activated photocatalyst Ag3PO4 and its significant antibacterial activity, Mater. Chem. Phys. 173 (2016) 385–394, https://doi.org/10.1016/j.matchemphys.2016.02.027.

[62] D. liu, X. Zhao, L. Song, S. Zhang, Synthesis, performance and action mechanism of carbon black/Ag3PO4 photocatalysts, Ceram. Int. 44 (12) (2018) 13712–13719, https://doi.org/10.1016/j.ceramint.2018.04.212.

[63] Y. Lin, et al., Spatial separation of photogenerated carriers and enhanced photocatalytic performance on Ag3PO4 catalysts via coupling with PPy and MWCNTs, Appl. Catal. B Environ. vol. 258, no. June (2019) 117969, https://doi.org/10.1016/j.apcatb.2019.117969.

[64] H. Yu, et al., Enhanced photocatalytic degradation of tetracycline under visible light by using a ternary photocatalyst of Ag3PO4/AgBr/g-C3N4 with dual Z-scheme heterojunction, Sep. Purif. Technol. 237 (2020) 116365, https://doi.org/10.1016/j.seppur.2019.116365.

[65] X. Guan, J. Shi, L. Guo, Ag 3 PO 4 photocatalyst : Hydrothermal preparation and enhanced O 2 evolution under visible-light irradiation, Int. J. Hydrogen Energy 38 (27) (2013) 11870–11877, https://doi.org/10.1016/j.ijhydene.2013.07.017.

[66] X. Song, R. Li, M. Xiang, S. Hong, K. Yao, Y. Huang, Morphology and photodegradation performance of Ag3PO4 prepared by (NH4)3PO4, (NH4)2HPO4 and NH4H2PO4, Ceram. Int. 43 (5) (2017) 4692–4701, https://doi.org/10.1016/j.ceramint.2016.12.124.

[67] J. Jin, et al., Oxygen-Vacancy-Rich BiO2- x/Ag3PO4/CNT Composite for Polycyclic Aromatic Hydrocarbons (PAHs) Removal via Visible and Near-Infrared Light Irradiation, Ind. Eng. Chem. Res. 59 (13) (2020) 5725–5735, https://doi.org/10.1021/acs.iecr.0c00232.

[68] R. Zhang *et al.*, "Photocatalytic Poly(vinylidene fluoride) membrane of Ag3PO4/GO/APTES for water treatment," *Colloids Surfaces A Physicochem. Eng. Asp.*, vol. 597, no. April, 2020, doi: 10.1016/j.colsurfa.2020.124779.

[69] P.J. Mafa, R. Patala, B.B. Mamba, D. Liu, J. Gui, A.T. Kuvarega, Plasmonic Ag3PO4/EG photoanode for visible light-driven photoelectrocatalytic degradation of diuretic drug, Chem. Eng. J. 393 (November) (2020) 124804, https://doi.org/10.1016/j.cej.2020.124804.

[70] R. Zhang, et al., Reduced Graphene Oxide-Doped Ag3PO4 Nanostructure as a High Efficiency Photocatalyst Under Visible Light, J. Inorg. Organomet. Polym. Mater. 30 (2) (2020) 543–553, https://doi.org/10.1007/s10904-019-01214-z.

[71] M. Thomas, S.K. Ghosh, K.C. George, Characterisation of nanostructured silver orthophosphate, Mater. Lett. 56 (4) (2002) 386–392, https://doi.org/10.1016/S0167-577X(02)00496-2.

[72] O.A.A. El-Shamy, H. Selim, A.S. Elkholy, R.S. Kamal, N.M. Saleh, N.E.A. Abd El-Sattar, Preparation of thiourea derivative incorporated Ag3PO4 core shell for enhancement of photocatalytic degradation performance of organic dye under visible radiation light, Sci. Rep. 14 (1) (2024) 1–12, https://doi.org/10.1038/s41598-024-62608-9.

[73] M. Ghiaci, M.E. Sedaghat, H. Aghaeia, A. Gilb, Synthesis of CdS- and ZnS-modified bentonite nanoparticles and their applications to the degradation of eosin B, J. Chem. Technol. Biotechnol. 84 (12) (2009) 1908–1915, https://doi.org/10.1002/jctb.2264.

[74] D.L. Wood, 0. 05–0. 08, Phys. Rev. B 5 (8) (1972) 3144–3151.

[75] Y. Xu, X. Zhang, Y. Zhang, J. Zhu, R. Zhu, "Nano flake Ag3PO4 enhanced photocatalytic activity of bisphenol A under visible light irradiation", *Colloids Interface*, Sci. Commun. vol. 37, no. June (2020) 100277, https://doi.org/10.1016/j.colcom.2020.100277.

[76] H. Lin, C.P. Huang, W. Li, C. Ni, S.I. Shah, Y.H. Tseng, Size dependency of nanocrystalline TiO2 on its optical property and photocatalytic reactivity exemplified by 2-chlorophenol, Appl. Catal. B Environ. 68 (1–2) (2006) 1–11, https://doi.org/10.1016/j.apcatb.2006.07.018.

[77] S. Suwanboon, P. Amornpitoksuk, N. Muensit, Dependence of photocatalytic activity on structural and optical properties of nanocrystalline ZnO powders, Ceram. Int. 37 (7) (2011) 2247–2253, https://doi.org/10.1016/j.ceramint.2011.03.016.

[78] L. Liu, P. Hu, Y. Li, W. An, J. Lu, W. Cui, P3HT-coated Ag 3 PO 4 core-shell structure for enhanced photocatalysis under visible light irradiation, Appl. Surf. Sci. 466 (2019) 928–936, https://doi.org/10.1016/j.apsusc.2018.10.112.

[79] Y. Xie, et al., Controlled synthesis and photocatalytic properties of rhombic dodecahedral Ag 3 PO 4 with high surface energy, Appl. Surf. Sci. 389 (2016) 56–66, https://doi.org/10.1016/j.apsusc.2016.07.088.

[80] F. Mu, et al., Construction of a novel Ag/Ag3PO4/MIL-68(In)-NH2 plasmonic heterojunction photocatalyst for high-efficiency photocatalysis, J. Mater. Sci. Technol. 101 (2022) 37–48, https://doi.org/10.1016/j.jmst.2021.05.059.

[81] R. Xiao-fang Li, Xian Li, X. Qiang Feng, Efficient Adsorption and Photocatalytic Degradation of Organic Pollutant by Ag3PO4/ZnO/Chitosan–Biochar Composites, Russ. J. Inorg. Chem. 68 (10) (2023) 1386–1398, https://doi.org/10.1134/S0036023623601307.

[82] S. Promnopas, et al., One-step microwave-hydrothermal synthesis of visible-light-driven Ag3PO4/LaPO4 photocatalyst induced by visible light irradiation, Chem. Phys. Lett. vol. 779, no. June (2021) 138883, https://doi.org/10.1016/j.cplett.2021.138883.

[83] P. Zhang, et al., Fabrication of MoS2QDs/Ag3PO4 photocatalyst for efficient visible light catalysis, Res. Chem. Intermed. 49 (11) (2023) 5029–5043, https://doi.org/10.1007/s11164-023-05113-4.

[84] L. Luo, Y. Li, J. Hou, Y. Yang, Visible photocatalysis and photostability of Ag 3 PO 4 photocatalyst, Appl. Surf. Sci. 319 (1) (2014) 332–338, https://doi.org/10.1016/j.apsusc.2014.04.154.

[85] P. Amornpitoksuk, K. Intarasuwan, S. Suwanboon, J. Baltrusaitis, Effect of phosphate salts (Na3PO4, Na 2HPO4, and NaH2PO4) on Ag 3PO4 morphology for photocatalytic dye degradation under visible light and toxicity of the degraded dye products, Ind. Eng. Chem. Res. 52 (49) (2013) 17369–17375, https://doi.org/10.1021/ie401821w.

[86] J. Ma, et al., Nanocomposite of attapulgite-Ag3PO4 for Orange II photodegradation, Appl. Catal. B Environ. 144 (1) (2014) 36–40, https://doi.org/10.1016/j.apcatb.2013.06.029.

[87] B. Akhsassi, et al., Enhanced photocatalytic activity of Zn3(PO4)2/ZnO composite semiconductor prepared by different methods, Chem. Phys. Lett. vol. 783, no. September (2021) 139046, https://doi.org/10.1016/j.cplett.2021.139046.

[88] I.M. Ibrahim, M.E. Moustafa, M.R. Abdelhamid, Effect of organic acids precursors on the morphology and size of ZrO2 nanoparticles for photocatalytic degradation of Orange G dye from aqueous solutions, J. Mol. Liq. 223 (2016) 741–748, https://doi.org/10.1016/j.molliq.2016.08.113.

[89] I. May-Lozano, M. Ramos-Reyes, M.R. López-Medina, G. Martínez-Delgadillo, S. A. Flores-Moreno, J. Hernández-Pérez, Effect of the Amount of Water in the Synthesis of B-TiO 2, Int. J. Photochem. 2014 (2014) 8.

[90] Z. Barzgari, A. Ghazizadeh, S.Z. Askari, Preparation of Mn-doped ZnO nanostructured for photocatalytic degradation of Orange G under solar light, Res. Chem. Intermed. 42 (5) (2016) 4303–4315, https://doi.org/10.1007/s11164-015-2276-y.

[91] M. Vinayagam, S. Ramachandran, V. Ramya, A. Sivasamy, Photocatalytic degradation of orange G dye using ZnO/biomass activated carbon nanocomposite, J. Environ. Chem. Eng. 6 (3) (2018) 3726–3734, https://doi.org/10.1016/j.jece.2017.06.005.

[92] C. Cai, J. Liu, Z. Zhang, Y. Zheng, H. Zhang, Visible light enhanced heterogeneous photo-degradation of Orange II by zinc ferrite (ZnFe2O4) catalyst with the assistance of persulfate, Sep. Purif. Technol. 165 (2016) 42–52, https://doi.org/10.1016/j.seppur.2016.03.026.

[93] N. Riaz, F.K. Chong, B.K. Dutta, Z.B. Man, M.S. Khan, E. Nurlaela, Photodegradation of Orange II under visible light using Cu-Ni/TiO 2: Effect of calcination temperature, Chem. Eng. J. 185–186 (2012) 108–119, https://doi.org/10.1016/j.cej.2012.01.052.

[94] F. Zhou, C. Yan, T. Liang, Q. Sun, H. Wang, Photocatalytic degradation of Orange G using sepiolite-TiO2 nanocomposites: Optimization of physicochemical parameters and kinetics studies, Chem. Eng. Sci. 183 (2018) 231–239, https://doi.org/10.1016/j.ces.2018.03.016.

[95] J. Sun, L. Qiao, S. Sun, G. Wang, Photocatalytic degradation of Orange G on nitrogen-doped TiO2 catalysts under visible light and sunlight irradiation, J. Hazard. Mater. 155 (1–2) (2008) 312–319, https://doi.org/10.1016/j.jhazmat.2007.11.062.

[96] A.I. Navarro-Aguilar, S. Obregón, D. Sanchez-Martinez, D.B. Hernández-Uresti, An efficient and stable WO3/g-C3N4 photocatalyst for ciprofloxacin and orange G degradation, J. Photochem. Photobiol. A Chem. vol. 384, no. August (2019) 112010, https://doi.org/10.1016/j.jphotochem.2019.112010.

[97] A.A. Al-Beladi, S.A. Kosa, R.A. Wahab, M.A. Salam, Removal of orange G dye from water using halloysite nanoclay-supported ZnO nanoparticles, Desalin. Water Treat. 196 (2020) 287–298, https://doi.org/10.5004/dwt.2020.25923.
[98] P. V. L. Photocatalytic, "Bimetallic Fe / Ti-Based Metal – Organic Framework for Persulfate-Assisted Visible Light Photocatalytic Degradation of Orange II," 2018.
[99] Y. El Jemli, M. Mansori, O. Gonzalez Diaz, A. Barakat, A. Solhy, K. Abdelouahdi, Controlling the growth of nanosized titaniaviapolymer gelation for photocatalytic applications, RSC Adv. 10 (33) (2020) 19443–19453, https://doi.org/10.1039/d0ra03312j.